COMPUTATIONAL TOOLS FOR IMAGE PROCESSING, INTEGRATION, AND VISUALIZATION OF SIMULTANEOUS OCT-FLIM IMAGES OF TISSUE

A Dissertation

by

JOSE DE JESUS RICO JIMENEZ

Submitted to the Office of Graduate and Professional Studies of
Texas A&M University
in partial fulfillment of the requirements for the degree of

DOCTOR OF PHILOSOPHY

Chair of Committee,	Javier Jo
Committee Members,	Brian Applegate
	Kristen Maitland
	Fred Clubb
Head of Department,	Anthony Guiseppi-Elie

December 2016

Major Subject: Biomedical Engineering

ABSTRACT

Multimodal imaging systems have emerged as robust methods for the characterization of atherosclerotic plaques and early diagnosis of oral cancer. Multispectral wide-field Fluorescence Lifetime Imaging Microscopy (FLIM) has been shown to be a capable optical imaging modality for biomedical diagnosis oral cancer. A fiber-based endoscope combined with an intensified charge-coupled device (ICCD) allows to collect and split the fluorescence emission into multiple bands, from which the fluorescence lifetime decay in each spectral channel can be calculated separately. However, for accurate calculations, it is necessary to gather multiple gates increasing the imaging time. Since this time is critical for real-time in vivo applications. This study presents a novel approach to using Rapid Lifetime Determination (RLD) methods to considerably shorten this time period.

Moreover, the use of a dual-modality system, incorporating Optical Coherence Tomography (OCT) and FLIM, which simultaneously characterizes 3-D tissue morphology and biochemical composition of tissue, leads to the development of robust computational tools for image processing, integration, and visualization of these imaging techniques. OCT-FLIM systems provide 3D structural and 2D biochemical tissue information, which the software tools developed in this work properly integrate to assist the image processing, characterization, and visualization of OCT-FLIM images of atherosclerotic plaques.

Additionally, plaque characterization is performed by visual assessment and requires a trained expert for interpretation of the large data sets. Here, we present two novel computational methods for automated intravascular (IV) OCT plaque characterization. The first method is based on the modeling of each A-line of an IV-OCT data set as a linear combination of a number of depth profiles. After estimating these depth profiles by means of an alternating least square optimization strategy, they are automatically classi-

fied to predefined tissue types based on their morphological characteristics. The second method is intended to automatically identify macrophage/foam cell clusters in atherosclerotic plaques. Vulnerable plaques are characterized by presenting a necrotic core below a thin fibrous cap, and extensive infiltration of macrophages/foam cells. Thus, the degree of macrophage accumulation is an indicator in determining plaque progression and probability of rupture. In this work, two texture features are introduced, the normalized standard deviation ratio (NSDRatio) and the entropy ratio (ENTRatio), to effectively classify areas in the plaque with macrophage/foam cell infiltration. Since this methodology has low complexity and computational cost, it could be implemented for in vivo real time identification of macrophage/foam cell presence.

DEDICATION

To my family and friends who encourage me to pursue this Ph.D program.

CONTRIBUTORS AND FUNDING SOURCES

Contributors

A dissertation committee consisting of Dr. Javier Jo (advisor), Dr. Brian Applegate, and Dr. Kristen Maitland of the Department of Biomedical Engineering and Dr. Fred Clubb of the Department of Veterinary Medicine and Biomedical Sciences.

The data analyzed for Sections 2 and 3 was provided by Dr. Brett Bouma and Dr. Martin Villiger form The Wellman Center for Photomedicine at the Massachusetts General Hospital. The data studied in Sections 4 and 6 was obtained in collaboration with Dr. Brian Applegate's reserch group, and Dr. Walton and Dr. Buja from the Cardiovascular Experimental Imaging and Therapeutics - Texas Heart Institute. The data used for Section 5 was aquired with a system developed in collaboration with Dr. Kristen Maitland's research group, and Dr. Y. Cheng and Dr. J. Wright from the Department of Diagnostic Sciences, Texas A&M Health Science Center - Baylor College of Dentistry.

Funding Sources

This graduate study was supported by the CONACyT fellowship, the dissertation fellowship from Texas A&M University, the National Heart, Lung, and Blood Institute (NHLBI) (1R01HL111361), and the National Institute of Biomedical Imaging and Bioengineering (NIBIB)(Center for Biomedical OCT Research and Translation, P41EB015903).

NOMENCLATURE

ENTRatio	Entropy Ratio
FLIM	Fluorescence Lifetime Imaging Microscopy
ICCD	Intensified Charge-Coupled Device
IT	Intimal-Thickening
IV-OCT	Intravascular OCT
LDA	Linear Discriminant Analysis
M/FC	Macrophage/Foam Cells
NSD	Normalized Standard Deviation
NSDRatio	Normalized Standard Deviation Ratio
OCT	Optical Coherence Tomography
OFDI	Optical Frequency Domain Imaging
ORLD	Optimized Rapid Lifetime Determination
PS-OFDI	Polarization-Sensitive OFDI
RLD	Rapid Lifetime Determination
SRLD	Standard Rapid Lifetime Determination
TCFA	Thin-Cap Fibroatheroma
VTK	Visualization Toolkit

TABLE OF CONTENTS

Page

LIST OF FIGURES

FIGURE Page

LIST OF TABLES

1. INTRODUCTION

This work was intended to provide a set of computational tools to assist the imaging and analysis procedures of OCT and FLIM techniques. The dissertation is divided in five sections describing a characterization method for the identification of fibrous and lipid plaques intravascular OCT imaging; a second method for the identification of macrophage/ foam cell clusters in intravascular OCT; a third classification method for the discrimination of macrophage/foam cell agglomerations in multimodal OCT-FLIM imaging of coronary arteries; an implementation of rapid lifetime algorithms to increase the imaging speed of a flexible FLIM endoscope; and a set of software tools for the integration and visualization of OCT and FLIM imaging of tissue.

Section 2 describes a characterization method for intravascular OCT images of atherosclerotic plaques based on the morphology of the A-line class profiles. This method estimates the profiles and abundances of the main A-line class profiles, the morphological features of each profile are extracted to be used in an LDA classifier. The artery tissue is classified in four different categories: Intimal-Thickening, Fibrotic, Fibrotic-Lipid, Superficial-Lipid.

Section 3 reports a methodology for the identification of macrophages/foam cells in intravascular OCT imaging. This method introduces two new concepts of texture features, the NSDRatio and the ENTRatio, based on the ratio of the calculation of the variability or randomness in those regions using the normalized standard deviation and the entropy. A simple threshold is used for a binary classification. The receiver operating characteristic analysis is used to find the optimum threshold and to evaluate the performance of the method. The proposed NSDRatio and ENTRatio features increase the sensitivity and specificity in the identification of M/FC clusters compared with the normalized standard deviation method.

Section 4 shows an approach for the discrimination of regions with macrophage/ foam cell presence in multimodal OCT-FLIM images of tissue. The identification of macrophage presence in OCT images is based on the methodology described in the second section. The identification of macrophage presence in FLIM images is based on the application of a simple threshold applied to the lifetime map of the second spectral channel centered at 494nm. A statistical analysis applied to OCT-FLIM images of human coronary arteries shows the performance of this method.

Section 5 demonstrates that the implementation of rapid lifetimes algorithms such as the standard rapid lifetime determination, the optimized rapid lifetime determination, and the four-gate FLIM methods increase the imaging speed to allow in vivo FLIM imaging of tissue. The drawback of this methods is that the accuracy is lower and the standard deviation is higher.

Section 6 presents a visualization software that combines image processing tools for the integration and visualization of OCT imaging. This software is capable of integrate 3D images from OCT showing morphology information and 2D images from FLIM showing biochemical composition of tissue. It includes the common image processing routines for OCT-FLIM imaging such as image enhancement, surface detection, denoising, and lumen removal. It allows to show different perspectives of the sample with effortless renderer manipulation and Swapping views from the volumetric to the sliced view.

2. AUTOMATIC CLASSIFICATION OF ATHEROSCLEROTIC PLAQUES IMAGED WITH INTRAVASCULAR OCT*

2.1 Introduction

Globally, atherosclerosis is the leading cause of death and morbidity. The different stages involved in atherosclerotic plaque formation must be studied and characterized in order to develop new therapies for atherosclerosis. In a stable plaque, the accumulation of collagen forming a fibrous plaque can lead to progressive stenosis, while in a vulnerable plaque, the build-up of lipids and necrotic core can lead to sudden thrombosis and heart attack [1]. Most vulnerable plaques are characterized by having a large necrotic core covered by a thin inflamed fibrous cap, the hallmarks of the thin cap fibroatheroma. To improve our understanding of the mechanisms that lead to a thrombotic event, it is relevant to characterize both the morphology and the composition of the plaque with the potential to identify the more deadly vulnerable plaques.

Since its development in 1991 and its implementation for vascular imaging in 1996 [2], OCT has shown high potential for imaging of atherosclerotic plaques. OCT has rapidly evolved in the past decade as a clinically useful diagnostic modality and has become very useful for intravascular (IV) imaging due its high spatial resolution and sensitivity [3, 4, 5, 6]. A standard nomenclature has been generated to provide a consensus in the usage guidelines, measurement methodology, and visual image interpretation criteria for IV-OCT image characterization [6]. Under this consensus, the normal vessel wall or intimal thickening is characterized by a highly backscattering or signal-rich intima layer, a low backscattering and signal-poor media layer, and a heterogeneous and highly backscat-

* Reprinted with permission from "Automatic classification of atherosclerotic plaques imaged with intravascular OCT" by J. J. Rico-Jimenez, D. U. Campos-Delgado, M. Villiger, K. Otsuka, B. E. Bouma, J. A. Jo. 2016. Biomed Opt Express 7(10), 4069-4085. Copyright [2016] by The Optical Society of America.

tering adventitia layer. High backscattering and homogeneous IV-OCT signal characterize a fibrous plaque. A calcific plaque is usually surrounded by fibrous tissue, and present a signal-poor region with sharply delineated borders. Superficial-Lipid plaques appear as a signal-poor region with poorly delineated borders and fast IV-OCT signal decay. An OCT thin-capped fibroatheroma presents a delineated necrotic core overlaid by a fibrous cap with a thickness less than a predetermined threshold. Macrophage accumulations are characterized as signal-rich regions with high standard deviation, distinct, and/or confluent punctate spots that surpass the intensity of background speckle noise.

Fibrous cap thickness is an important parameter of plaque vulnerability, which IV-OCT is able to accurately assess, owing to its high axial resolution [7]. However, visual assessment [8, 9, 10] of OCT cross-sectional images (B-scans) is cumbersome, extremely time consuming, and requires trained experts to classify diverse features present in each stage of the disease development. Furthermore, the inherent effect of speckle and the scattering attenuation of the optical scheme limit the direct interpretation of OCT images.

Although OCT is becoming very popular for intravascular imaging of atherosclerotic plaques, a single pullback generates hundreds of B-scans; interpreting this large amount of data makes the characterization process very tedious. To overcome these difficulties, different automatic characterization methods have been developed based on either texture segmentation or attenuation analysis. Random Forests classification using intensity and texture-based features extracted from regions in the B-scan corresponding to the atherosclerotic plaque area has been used to classify four types of plaque: calcium, lipid pool, fibrous tissue and mixed plaque [11]. The main limitation of this method is the identification of lipid pool and mixed plaque since the classification accuracy reported was lower than 80%. A texture based segmentation method uses Spatial Gray Level Dependence Matrices Method, second order statistical texture features extraction, to automatically detect plaque and non plaque regions from OCT images [12]. The drawback of this method is

the clusters, distance metric, initialization of cluster centroids and convergence criterion parameters that need to be set correctly to ensure that the algorithm converges and produces satisfying results. Even so, it may not reliably detect all the different plaque types. Windows of variable length can be used to estimate the backscatter and the extinction coefficients from transverse sections resulting in a quantitative estimation of these coefficients for every A-line [13]. This approach was intended to identify five different tissue types: fibrous and smooth muscle cells, early necrotic core, advanced necrotic core, calcification, and hemorrhage. Yet, it is prone to erroneously compute the backscatter coefficient due tissue heterogeneity and the lack of an intensity calibration. Similarly, estimation of the optical attenuation coefficient combined with a supervised classification of image pixels according to textural features was proposed to improve the automated and systematic characterization with IV-OCT of the following atherosclerotic plaque types: fibrotic, calcified, and lipid-rich; yet, this procedure requires user input for the selection of regions of interest (ROIs) for plaque assessment [14]. Recently, a method was proposed to estimate the attenuation coefficient as a function of depth for each A-line in order to to identify calcifications, necrotic core, and mixed plaque [15]. The estimation of optical parameters from volumes of interest has also been attempted in order to classify calcified, fibrotic and lipid plaques; however, this volumetric analysis can be computationally expensive [16]. A combined depth resolved spectral and attenuation model showed the potential of predicting lipid content in OCT images of atherosclerotic plaques[17]. This classification method is based on a quadratic discriminant analysis model utilized on phantoms of known chemical mixtures, such as collagen, calcium and cholesterol, as well as simulated tissue of a lipid-rich plaque. However, the inherent heterogeneity of the fibroatheromas might affect the performance of the proposed approach. A novel method intended for lipid-rich plaque characterization in IV-OCT images used the spectroscopic absorption properties of lipids to evaluate lipid phantom models and in vivo atherosclerotic rabbit models[18].

In this study the Gaussian center of mass was used as a metric to visualize the property of the spectrum with a high sensitivity, specificity, and correlation of 94.3%, 76.7%, and R=0.8572, respectively. However, this method focused only in the composition of lipids, yet the heterogeneous plaque composition must be evaluated for further validation. A recent study have showed the potential birefringence images of polarization-sensitive optical frequency domain imaging (PS-OFDI) as a source of contrast to evaluate tissue composition[19]. Birefringence is elevated in areas with thick collagen fibers or smooth muscle cells, while in the fibrous cap region both at the rupture site and proximally present low birefringence. This optical tissue property can be used as a feature for an automated computational characterization method.

In this paper, we present a novel computational method for plaque tissue characterization that does not require estimating optical properties. Instead, this method allows for tissue characterization based on the intrinsic morphological characteristics of the A-lines in IV-OCT scans. Since this method is fully automated, it has the potential for high throughput atherosclerotic plaque assessment.

2.2 Methods

The main idea behind our method for automated plaque characterization is modeling each A-line of the IV-OCT B-scan as a linear combination of N depth profiles ($\mathbf{p}_1, \ldots, \mathbf{p}_N$). These profiles are estimated anew from each B-scan or a set of consecutive B-scans, and are then further classified to a specific tissue type, based on morphological features. This is illustrated in Fig. 2.1, in which two profiles ($\mathbf{p}_1, \mathbf{p}_2$) estimated from the sample B-scan are modeling any given A-line of the B-scan. In this particular example, the blue profile resembles an Intimal-Thickening profile having two prominent peaks and one valley, which represent the intima, media, and adventitia layers; those peaks are faded in the red profile due to thickening caused by fibrous tissue build up, while the decay of the signal

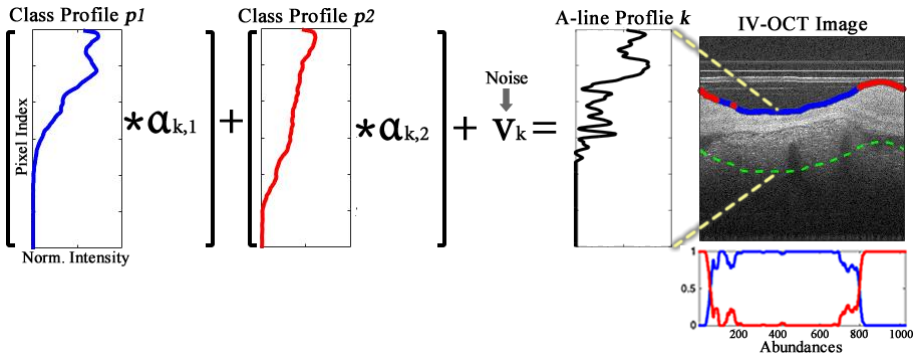

Figure 2.1: Illustration of the *k-th* A-line profile (black) being modeled as the linear combination of two main profiles ($\mathbf{p}_1$ in blue and $\mathbf{p}_2$ in red) each with corresponding abundances ($\alpha_{k,1}, \alpha_{k,2}$) for that particular A-line, plus a noise component $\mathbf{v}_k$. The color on the lumen of the OCT image indicate the most dominant class at that specific A-line. The dotted green line marks the maximum depth considered for the profile in the region of interest. The right-bottom plot depicts the abundances of both profiles at each A-line.

is slower due to the characteristic high backscattering of fibrotic plaque. Once the profiles are estimated for a given B-scan, they are automatically classified into one of several potential tissue classes based on a set of morphological features. Since the *k-th* A-line in the B-scan has a characteristic weight or abundance $\alpha_{k,n}$ for each profile $\mathbf{p}_n$, their magnitudes can be used to assign each A-line to a specific tissue type. This is illustrated in Fig. 2.1, in which a sample A-line at the position $k = 400$ is composed by the Blue-class profile times the weight or abundance $\alpha_{k,1}$, plus the Red-class profile times the abundance $\alpha_{k,2}$, with the addition of noise $\mathbf{v}_k$. Since the Blue-class profile has the most dominant abundance, the resulting A-line profile must be more akin to this class. Thus, the lumen is color-coded as blue indicating Intimal-Thickening in that particular A-line position. A detailed description of our proposed methodology, as summarized in Fig. 2.2, is presented below.

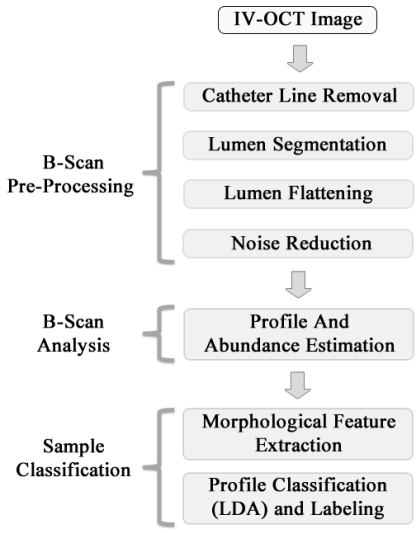

Figure 2.2: Block diagram of the automatic classification process.

2.2.1 B-scan pre-processing

Each IV-OCT B-scan was first pre-processed as follows. As shown in Fig. 2.3, the lines produced by the catheter ball lens and sheath signal are removed, and the lumen surface is segmented. Next, the lumen surface is flattened using an elastic transformation method [20] and a fix amount of pixels are selected from the lumen surface to certain depth where the signal has decayed to the background (dotted line in Fig. 2.3); a constant depth of 300 pixels (300×4.8 μm = 1,440 μm, see section 2.2.5 for system resolution details) was used throughout this study. An Entropy filter with a window size of 5×5 pixels is applied to the segmented image to reduce the speckle effect; although other spatial filters such as Median, Wiener, Lee, and Frost with different window sizes can be also used [21, 22]. A logarithmic transformation looks to enhance the small details in the signals, which is especially important for visualization purposes. However, since we are applying a linear combination model of the profiles by A-line, the processing of the B-scans in logarithmic scale would induce a multiplicative effect in the linear scale, which is not suitable for the

posterior interpretation and classification stage. As a result, the B-scan pre-processing is performed on the normalized linear signal (0-1) and the Log-compressed image is used only for visualization purposes.

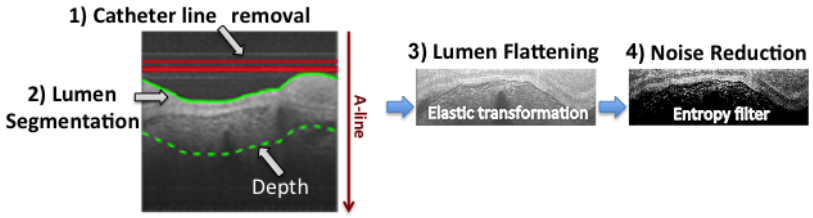

Figure 2.3: B-scan pre-processing steps.

2.2.2 B-scan analysis

Our proposed B-scan analysis is based on the following considerations:

i) A set of OCT A-lines can be represented as a non-negative matrix of L pixels by K A-lines (In this study the set of A-lines was taken from 9 consecutive B-scans).

ii) Each measured A-line is composed by a linear mixture of N profiles $(\mathbf{p}_1, \ldots, \mathbf{p}_N)$, and these profiles are invariant over the whole set of A-lines.

Therefore, considering a linear mixture of profiles at the *k-th* measured A-line $\mathbf{y}_k$ with random noise $\mathbf{v}_k$, the following observation model is assumed:

$$\mathbf{y}_k = \sum_{n=1}^{N} \alpha_{k,n}\mathbf{p}_n + \mathbf{v}_k; \qquad \sum_{n=1}^{N} \alpha_{k,n} = 1 \tag{2.1}$$

where the coefficients $\alpha_{k,n} > 0$ are interpreted as the abundance or weight parameters of the *n-th* profile at the *k-th* A-line. By considering a matrix notation, the observation model

can be written as

$$\mathbf{Y} = \mathbf{PA} + \mathbf{V} \tag{2.2}$$

where $\mathbf{Y} = [\mathbf{y}_1 \ \ldots \ \mathbf{y}_K]$ is a matrix of size $L \times K$, representing the set of measured A-lines, $\mathbf{P} = [\mathbf{p}_1 \ \ldots \ \mathbf{p}_N]$ is a matrix of size $L \times N$, representing the unknown profiles, $\mathbf{A} = [\boldsymbol{\alpha}_1 \ \ldots \ \boldsymbol{\alpha}_K]$ is a matrix of size $N \times K$ containing the unknown abundances, and $\mathbf{V} = [\mathbf{v}_1 \ \ldots \ \mathbf{v}_K]$ is the matrix gathering noise components. In this representation, the vector of abundances at the $k-th$ A-line is denoted as $\boldsymbol{\alpha}_k = [\alpha_{k,1} \ \ldots \alpha_{k,N}]^\top$. In this way, the simultaneous estimation of the unknown sets of profiles $\mathbf{P}$ and abundances $\mathbf{A}$ is formulated as a nonlinear quadratic optimization process: [23, 24, 25]

$$\min_{P,A} \frac{1}{2}\|\mathbf{Y} - \mathbf{PA}\|_F^2 + \rho \sum_{i=1}^{N-1} \sum_{j=i+1}^{N} \|\mathbf{p}_i - \mathbf{p}_j\|^2 - \mu\|\mathbf{A}\|_F^2 \tag{2.3}$$

with the following restrictions

$$\mathbf{P} \geq 0, \quad \mathbf{A} \geq 0, \quad \mathbf{A}^\top \mathbf{1} = \mathbf{1} \tag{2.4}$$

i.e. $\mathbf{A}^\top \mathbf{1} = \mathbf{1}$ is equivalent to normalization condition of each column of matrix $\mathbf{A}$ as required by (1). This optimization problem is nonlinear in the product of the matrices $\mathbf{P}$ and $\mathbf{A}$, so an alternating least squares strategy is pursued to find the optimal solutions [26, 27, 28].

The first term in (2.3), is related to the approximation error by the observation model in (2); the second term is a regularization component in the cost function linked to the estimated profiles that penalizes the distance among them by using the weight $\rho > 0$; finally the last term is another regularization component now focused on the abundances that maximizes its values by A-line and this condition is controlled by the weight $\mu > 0$. Since the abundances are always positive and normalize to one per A-line, the last term

in (2.3), could produce a low entropy condition in the estimated abundances. In this way, the tradeoff between reducing the approximation error, controlling the distance among the estimated profiles or achieving a low entropy condition is regulated by the parameters ρ and μ.

This alternating least squares strategy begins with a matrix $\mathbf{P_0}$ that is initially defined for the iterative scheme. For this initialization process, the approach in [26] is followed, where the A-line with the largest energy in the B-scan is selected, as well as the A-line with the largest norm error with respect to the first one. Then, the system is solved for $\mathbf{A}$. Once $\mathbf{A}$ is found, the system is solved again for $\mathbf{P}$, and so on. Fixing either $\mathbf{P}$ or $\mathbf{A}$ in (2.3), the optimization problem becomes quadratic and it is solved over a convex domain. Nevertheless, the alternating least squares iteration can only assure convergence to a local minimum.

2.2.3 Automated profile classification

Once the profiles $(\mathbf{p}_1, \ldots, \mathbf{p}_N)$ and their abundances $(\boldsymbol{\alpha}_1, \ldots, \boldsymbol{\alpha}_K)$ are estimated, the resulting profiles are automatically classified and labeled to identify four different tissue types: *Intimal-Thickening (IT)*, *Fibrotic*, *Superficial-Lipid*, and *Fibrotic-Lipid*. To achieve this, each profile $\mathbf{p}_n$ is normalized to its maximum intensity value and a set of morphological features are estimated from it, as summarized in Table 2.1. The Intimal-Thickening profiles are identified based on the first four features in Table 2.1, and are characterized as having two prominent peaks and one valley with restricted widths and within the first part of the profile (blue region in Fig. 2.4, before the signal decay). If a profile is not identified as Intimal-Thickening based on the previous criteria, it is further classified into one of the other tissue types based on a Linear Discriminant Analysis (LDA) algorithm that uses the remaining morphological features defined in Table 2.1.

From all the morphological features explored and summarized in Table 2.1, only the

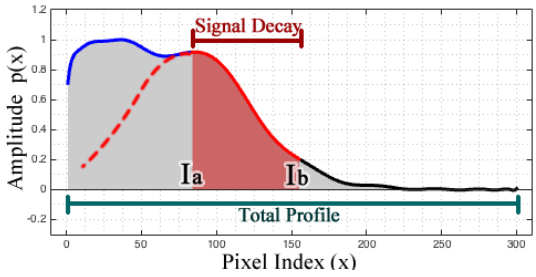

Figure 2.4: Profiles partition for feature extraction. The profile is divided into two sections: first for the region of the profile that is not highly attenuated (blue line) and second for the part where the most significant signal decay occurs (red solid line).

features marked with an (*) were used in the LDA classifier. These features were selected based on the exhaustive search strategy described in section 2.3.3. The first feature is the Goodness-of-fit (GOF) of a single term Gaussian model applied only to the signal decay section. The assumption is that the attenuation of lipids resembles a Gaussian model (red line in Fig. 2.4); thus, the GOF should be better (lower values) for the Superficial-Lipid and Fibrotic-Lipid profiles than for the Fibrotic profiles. The second feature is the index of the end of the signal decay, point I_b in the second section, indicating the signal has decreased to a value close to the background. The third feature is the area under the signal decay (A_R). The fourth feature is the area under the total profile signal (A_T). The last features are taken from the coefficients of a second polynomial fitting to the signal decay section, which assess the nonlinearity of the signal decay. Finally, once the profiles are classified and labeled, each A-line is linked to a specific label that was assigned to the profile with the highest abundance at that specific A-line.

2.2.4 Automated sample classification

In the context of sample level classification, the method evaluates whether or not a sample has accumulation of lipids. Thus, samples containing any profile classified as Superficial-Lipid or Fibrotic-Lipid are catalogued as Lipid-containing plaques; likewise,

Table 2.1: Profile morphological features.

Feature	Description
η	Number of prominent peaks
$\omega(Peak_n)$	Width of the *n-th* peak
$\psi(Peak_n)$	Location of the *n-th* peak
$\phi(Peak_n)$	Prominence of the *n-th* peak
$\chi^2 = \sum \frac{(p-\hat{p})}{\hat{p}}; \quad \hat{p}(x) = ae^{-\frac{(x-b)^2}{2c^2}}$	GOF of Gaussian fit of the signal decay *
I_a	Index of the beginning of the signal decay
I_b	Index of the end of the signal decay *
$d = \lvert I_a - I_b \rvert$	Distance from I_a to I_b
$A_R = \int_{I_a}^{I_b} p(x)dx$	Area under the signal signal decay *
$A_T = \int_1^N p(x)dx$	Area under the total profile signal *
$C(x) = c_1x^2 + c_2x + c_3$	Quadratic polynomial fitting *

sample containing only profiles classified as Intimal-Thickening or Fibrotic are attributed a No-Lipid classification. The algorithm highlights only the segments of the lumen where lipids are detected.

2.2.5 Database

Cadaveric human coronary arteries were imaged with a fiber-based intravascular Optical Frequency Domain Imaging (OFDI) system [3, 29], having a swept range of 115 nm, centered at 1320 nm and a repetition rate of 54 kHz; resulting in axial and lateral resolutions of 9.4 μm and 30 μm, respectively. It is important to state that this system takes polarization sensitive measurements, detecting two orthogonal polarization channels in parallel, and alternating the polarization state of the light incident on the sample in between A-lines. The sum of the squared norm of the complex-valued tomogram of each channel was computed, ignoring the modulation of the polarization states in between A-

lines. The database consisted of a total of 57 datasets of IV-OCT images, each consisting of 9 consecutive frames spaced by 100 μm in the longitudinal dimension. Each frame consists of 1024 axial depth-points and 1024 A-lines, corresponding to an angular sampling step of 0.35°. The axial resolution was 4.8 μm, assuming a refractive index of 1.34 of the tissue, for a total depth of 1024×4.8 μm = 4915.2 μm. The fifth of the 9 frames (central frame) was matched with one histological section, stained with Massons Trichrome.

2.2.6 Validation

Each histological section was visually assessed, blinded to the IV-OCT images, and the lumen was partitioned into segments, labeled as one of the following tissue types: Intimal-Thickening, Fibrous, Fibro-lipid, or Superficial-Lipid. The two, N=2, most abundant tissue types found in histopathology served as the ground-truth for training of the LDA classifier, to be predicted by the morphological features of the estimated profiles found in the corresponding IV-OCT data set. For sample-level classification, sections that contained any amount of lipid (at least 25% of the tissue lumen) were classified as Lipid-containing. Only sections without any Fibro-Lipid or Superficial-Lipid segments were classified as No-lipid. Analogously, a trained IV-OCT observer, blinded to the histopathology, classified all the IV-OCT cross-sections, by segmenting them into the same tissue categories, and for the sample-level classification, any lipid segment resulted in a plaque to be attributed to the Lipid-containing category. The automatic sample-level classification was compared to both the visual IV-OCT and histopathological diagnosis. The performance of the classification method was quantified with a leave-one-out-validation strategy on the entire histopathology data-base. For each iteration of the leave-one-out validation, one dataset was assigned for testing, and the other 56 data sets for training.

2.3 Results

In this section, we present the results of applying the proposed method to the aforementioned database assuming the presence of two most significant profiles (N=2) per B-scan or volume. In fact, N can take values > 2, however, if the number of profiles is too large, the decomposition algorithm could estimate profiles that are either not linearly independent or with insignificant abundances throughout the B-scan. The results presented here were obtained using the 9 consecutive B-scans for each histopathology section as input. The A-lines of the 9 B-scans, 1024 A-lines each, were appended together to form one single set of 9,216 A-lines.

2.3.1 B-scan pre-processing results

In the preprocessing stage, the following common speckle noise reduction filters were assessed with the IV-OCT images: Entropy, Median, Wiener, Lee, and Frost. Figure

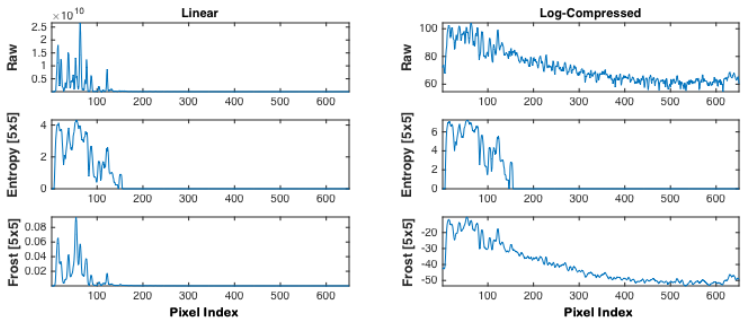

Figure 2.5: Comparison of an A-line signal after the Entropy and Frost filters were applied using a window size of 5×5. The first column shows the linear signal, while the second column shows the log-compressed version. The raw Linear and Log-compressed signals are plotted as reference in the first row, the second row shows the Entropy filtered A-line, and the third row depicts the Frost filtered version.

2.5 shows a comparison of an A-line signal after applying the Entropy and Frost speckle

reduction filters to an IV-OCT image. The first and second columns display plots of the linear and Log-compressed signal, respectively, for the raw and filtered signals. The first row shows the raw signal, the second row shows the result of applying the Entropy filter using a window of 5×5, and the last row shows the analogous version filtered with Frost. The Median, Wiener, and Lee filters are not shown in the figure since they produce similar results to the Frost filter. It is noticeable that raw Log-compressed image amplifies the signal from the sample but also from the background, while the Entropy minimizes the speckle and amplifies the signal from the sample, while suppressing the background signal. The Frost filter reduces the speckle noise, however, the background signal is not reduced significantly. Hence, for simplicity, speed, and efficiency, the Entropy filter with a size of 5×5 was adopted for this study.

2.3.2 B-scan analysis results

In the B-scan analysis step, the parameters ρ and μ were tuned to determine their optimal values. As stated in section 2.2.2, changes in ρ values directly affect the difference between the profiles, hence keeping this parameter to lower values leads to more distinct profiles. Similarly, μ controls the amplitude relation among the abundances. However, selecting the right scaling depends on the problem at hand, by the formulation of the quadratic optimization in (2.3), and this parameter is selected as $\mu = \mu_0 \ \lambda_{min}(\mathbf{P}^\top \mathbf{P})$, where $\lambda_{min}(\cdot)$ denotes the minimum eigenvalue of the matrix. As a consequence, $\mu_0 \in (0, 1)$ to avoid a singular problem during the computation of the abundances. Then, as shown in Fig. 2.6, the magnitudes of the abundances $\alpha_{k,n}$ separate with larger values of μ_0. For the analysis presented here, ρ was set to 0.25 to coerce the resultant profiles to be different to each other, while μ_0 was set to an intermediate value of 0.6 to maintain a balanced separation between abundances.

Figure 2.7 shows an example of the typical profile morphology for each of the four

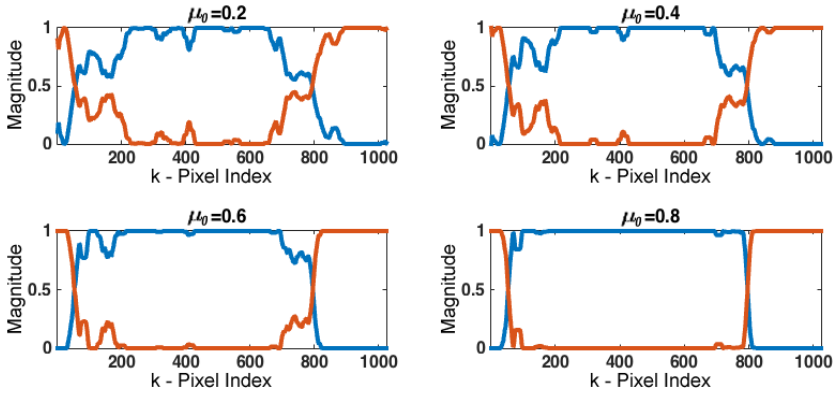

Figure 2.6: Abundances estimated with different μ_0 values. By increasing the values of μ_0, the magnitudes of the abundances $\alpha_{k,n}$ separate; e.g. at the A-line $k = 200$ the higher abundance (blue) increases while the lower abundance (orange) decreases separating them from each other.

main classes; a color code is used to differentiate each class. It was found that for Intimal-Thickening profiles, green plot in Fig. 2.7, the main characteristics are the two prominent peaks and one valley within the first 90 pixels. For the Fibrotic profiles (blue), the signal decays slower due to high scattering, while in Superficial-Lipid profiles (red) the decay is faster due high attenuation. For the Fibrotic-Lipid profiles (cyan), the first segment of the profile resembles the first part of a Fibrotic profile and the second part is very similar to the decay of the Superficial-Lipid class.

2.3.3 Morphological features selection results

The feature selection was based on an exhaustive search strategy, which selects the combination of features, described in Table 2.1, that leads to the higher classification accuracy estimated following a leave-one-out validation on the entire database. Thus, other features that were considered, such as index of the beginning of the signal decay (I_a), and the distance (d) from I_a to I_b, were discarded using this strategy.

Figure 2.8 shows a comparison of the distribution between the features described in section 2.2.3. The GOF of Gaussian fit (χ^2) values for Fibrotic profile are significantly

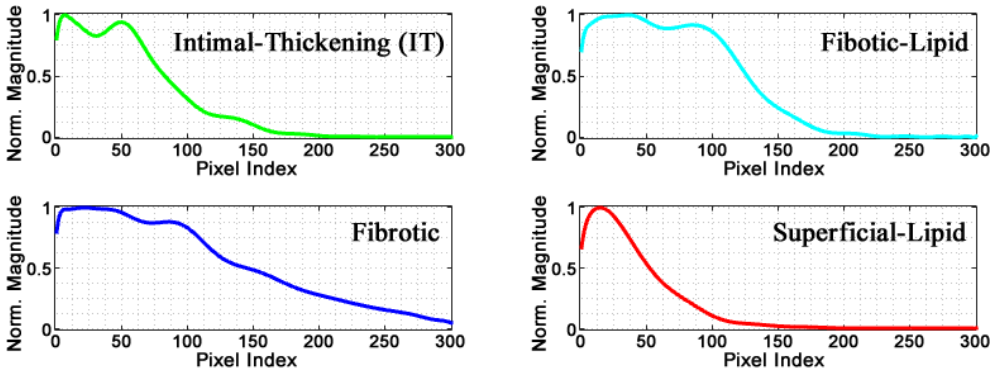

Figure 2.7: Typical morphology of different class profiles.

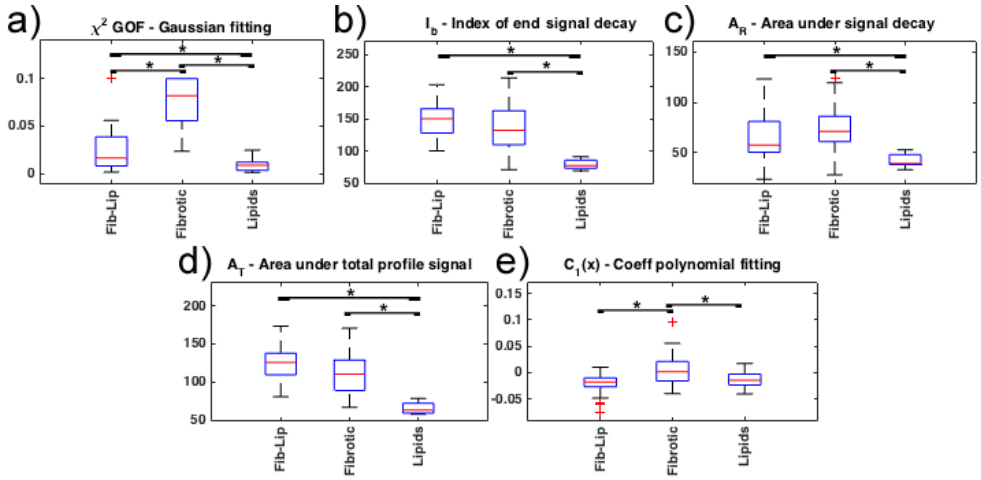

Figure 2.8: Comparison of features considered for the LDA classification. Multiple comparison with Bonferroni correction ($p < 0.05$).

higher (worse Gaussian fitting) than for Superficial-Lipid and Fibrotic-Lipid profiles. This is expected, since a better Gaussian fitting of the signal decay region was observed for the Superficial-Lipid and Fibrotic-Lipid profiles (Fig. 2.8(a)). The index of the end of the signal decay (I_b) shows lower values for Superficial-Lipid profiles than both Fibrotic-Lipid and Fibrotic profiles due to higher attenuation of Superficial-Lipid profiles (Fig. 2.8(b)). For the signal decay area (A_R), Fibrotic and Fibrotic-Lipid profiles exhibit larger

areas as the result of a slower decay. On the contrary, Superficial-Lipid profiles present significantly lower signal decay area due to high signal attenuation (Fig. 2.8(c)). Similarly, the total area A_T is higher for Fibrotic-Lipid and Fibrotic than Superficial-Lipid profiles (Fig. 2.8(d)). The values for the quadratic coefficient of the polynomial fitting ($C_1(x)$) are close to zero for Fibrotic and different from zero for Superficial-Lipid and Fibrotic-Lipid profiles. Thus, Fibrotic profiles can be closely fitted to a linear function, while Superficial-Lipid and Fibrotic-Lipid profiles can be fitted to a quadratic function (Fig. 2.8(e)).

2.3.4 Profile classification results

For the profile classification stage, the morphological features were analyzed to select those that will be used in the LDA classifier. The LDA classifier was tested using leave-one-out validation for the following types of discriminant function: Linear, Diagonal-linear, Quadratic, Diagonal-quadratic, and Mahalanobis. According to our testing, the Linear, Diagonal-linear, Quadratic, Diagonal-quadratic, and Mahalanobis led to an accuracy of 83.6%, 82.7%, 85.4%, 88.2%, and 85.4%, respectively, from which the Diagonal-quadratic gave the highest accuracy. Finally, each A-line is color-labeled in accordance with the classified profile with highest abundance.

The results of the classification method applied to three datasets characterized by histopathology as having regions corresponding to Intimal-Thickening, Fibrotic, Fibrotic-Lipid, and/or Superficial-Lipid plaques are shown in Figures 2.9-2.11. In each of these figures, the estimated profiles ($\mathbf{p}_n$) and abundances ($\alpha_{k,n}$) are shown on the top-left and bottom-left panels. The two profiles are color-coded based on the result of the automated classification as either Intimal-Thickening (green), Fibrotic (blue), Fibrotic-Lipid (cyan), or Superficial-Lipid (red). The middle-left panel shows the corresponding B-scan in Cartesian representation, in which the lumen is also color-coded based on the most dominant abundance for each A-line. The right panel shows the corresponding histopathology sec-

tion, in which the lumen is also color-coded based on the histopathological evaluation.

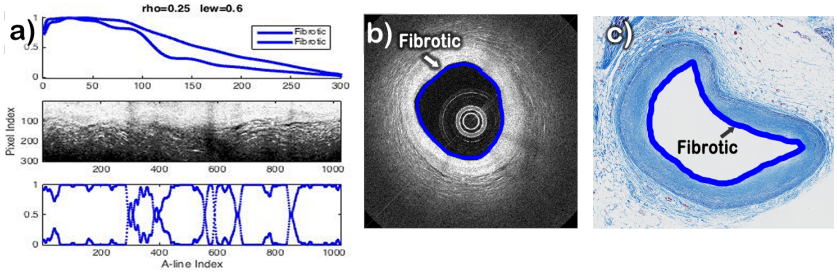

Figure 2.9: Automatic classification of a sample characterized by histopathology as being a Fibrotic plaque. a) Profiles plot (top), IV-OCT image with lumen flattened (center), and Abundances plot (Bottom); b) IV-OCT image with the lumen automatically colored according to the automatic classification; c) histological with the lumen colored manually according to the histological classification.

The results of the B-scan analysis for the case of a Fibrotic plaque are shown in Fig. 2.9(a). The B-scan image (Fig. 2.9(b)) exhibits high intensity and low attenuation for all the artery tissue, which indicates that only Fibrotic plaque is present. Since both profiles were classified as Fibrotic, the lumen was color coded blue all around in the B-scan, as shown in Fig. 2.9(b). The corresponding histology section (Fig. 2.9(c)) clearly indicates a homogeneous fibrotic plaque with no apparent lipid accumulation.

The results of the B-scan analysis for a particular sample presenting both Superficial-Lipid and Fibrotic-Lipid regions are shown in Fig. 2.10. The two profiles estimated from this B-scan are shown in Fig. 2.10(a). The red profile showed an immediate fast decay and was correctly classified as a Superficial-Lipid profile. The cyan profile showed an initial low attenuation region followed by a fast decay and was correctly classified as a Fibrotic-Lipid profile. The B-scan (Fig. 2.10(b)) illustrates areas with high attenuation at deeper depths and higher attenuation close to the surface suggesting the presence of

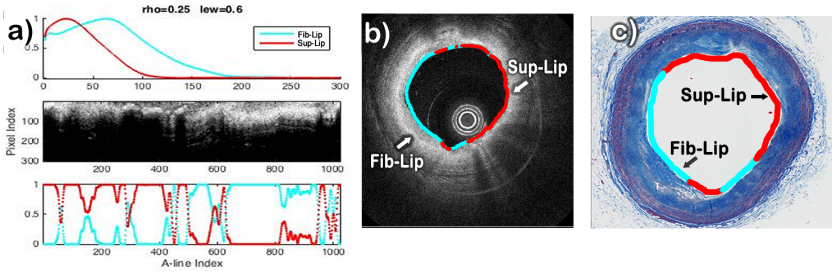

Figure 2.10: Automatic classification of a sample having regions of Superficial-Lipid and Fibrotic-Lipid plaques. a) Profiles plot (top), IV-OCT image with lumen flattened (center), and Abundances plot (Bottom); b) IV-OCT image with the lumen automatically colored according to the automatic classification; c) histological with the lumen colored manually according to the histological classification.

a mix of Fibrotic-Lipid and Superficial-Lipid areas, respectively. The lumen was color-coded based on the values of the estimated abundances as either Fibrotic-Lipid (cyan) or Superficial-Lipid profiles (red), as shown in the B-scan (Fig. 2.10(b)). The corresponding histology section (Fig. 2.10(c)) clearly indicates various regions with superficial and deep accumulation of lipids.

The results of the B-scan analysis for a plaque having both Intimal-Thickening and Fibrotic-Lipid regions are shown in Fig. 2.11. The two profiles estimated from this B-scan are shown in Fig. 2.11(a). The green profile showed two prominent peaks and one valley and was correctly classified as a Intimal-Thickening profile. The cyan profile showed an initial low attenuation region followed by a fast decay and was correctly classified as a Fibrotic-Lipid profile. In fact, the two profiles in Fig. 2.10(a) and the second profile (cyan) in Fig. 2.11(a) have very similar signal decay. The B-scan shows two distinct areas, in which the three artery layers are noticeable in one side of the artery and the other side has attenuation at certain depth where fibrotic tissue and lipids are mixed. The lumen was color-coded based on the values of the estimated abundances as either Intimal-Thickening (green) or Fibrotic-Lipid profiles (cyan), as shown in the B-scan (Fig. 2.11(b)). The

corresponding histology section (Fig. 2.11(c)) clearly indicates one Intimal-Thickening area and a fibrotic plaque with deep lipid accumulations.

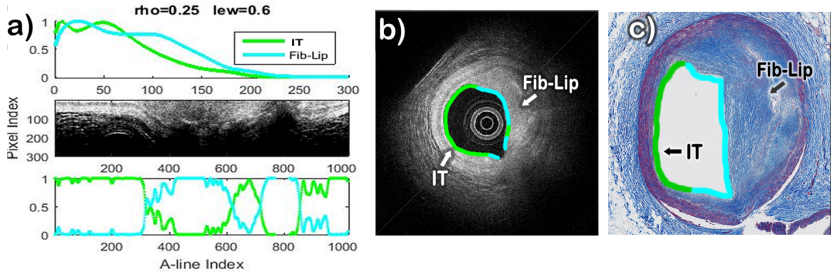

Figure 2.11: Automatic classification of a sample having regions corresponding to Intimal-Thickening (IT) and Fibrotic-Lipid. a) Profiles plot (top), IV-OCT image with lumen flattened (center), and Abundances plot (Bottom); b) IV-OCT image with the lumen automatically colored according to the automatic classification; c) histological with the lumen colored manually according to the histological classification.

The performance of the automated profile classification method assessed following a leave-one-out validation approach is summarized by the confusion matrix in Table 2.2. In our evaluation, the overall accuracy for this classification tests was 88.2%. The sensitivity and specificity for both the Fibrotic and Fibrotic-Lipid classes were approximately 84% and 90%, respectively. The sensitivity and specificity for both the Intimal-Thickening and Superficial-Lipid classes were 100%.

Table 2.2: Profile level confusion matrix.

		Leave-One-Out Classification					
		IT	Fib-Lip	Fibrotic	Sup-Lipid	Sensitivity %	Specificity %
Histo-pathology	IT	13	0	0	0	100	100
	Fib-Lip	0	39	7	0	84.8	90.6
	Fibrotic	0	6	30	0	83.3	90.5
	Sup-Lipid	0	0	0	15	100	100

Notice that in Table 2 there are a total of 110 profiles and 114 where expected from 57 samples. This method tries to find two profiles, N=2, from each sample, yet the estimated profiles are compared at each iteration of the alternating least squares to decide if they are alike so they can be considered as only one class. Thus, if a sample has only one class and the two estimated profiles are similar to certain extent, the result would be a single profile for that dataset (in Fig. 2.9, the two profiles did not match this criterion and, therefore, the method gave two different fibrotic profiles as result). In this database, there were 53 samples with two profiles (106 profiles) and 4 samples with only one profile; most of these cases came from datasets having only Intimal-Thickening or Fibrous tissue having similar thickness through all the artery section.

2.3.5 Sample classification results

In the context of sample level classification, the method evaluated whether or not a sample had accumulation of lipids. Thus, either a Superficial-Lipid profile or a Fibrotic-Lipid profile counts as Lipid-containing classification.

The visual classification provided by the IV-OCT observer was compared to the histopathological gold standard classification leading to the confusion matrix in Table 2.3 and exhibiting and accuracy of 80.7%. This classification showed sensitivity of 77.3% and specificity of 92.3% for detecting lipid plaques.

Table 2.3: Visual sample level classification confusion matrix.

		Visual Classification			
		Lipids	No Lipids	Sensitivity %	Specificity %
Histopathology	Lipids	34	10	77.3	92.3
	No Lipids	1	12		

Table 2.4 shows the confusion matrix for the automatic sample level classification with

an accuracy of 85.6%. The sensitivity and specificity for detecting plaque with accumulation of lipids were 86.4% and 84.6%, respectively.

Table 2.4: Automatic sample level classification confusion matrix.

		Leave-One-Out classification			
		Lipids	No Lipids	Sensitivity %	Specificity %
Histopathology	Lipids	38	6	86.4	84.6
	No Lipids	2	11		

For this case, the proposed classification algorithm automatically plots a line only on a specific section of the lumen where lipids where detected, as shown in Figure 2.12. In these examples, the proposed algorithm draws a cyan and red line on the lumen of the arteries in the two first IV-OCT images (*a* and *b*) having Fibrotic-Lipid and Superficial-Lipid plaques build up, respectively. For these cases, it is noticeable that the histological images show white areas revealing he presence of extracellular lipids and/or foam cells. The last IV-OCT image (*c*) corresponding to an artery with Fibrous plaque and intimal thickening does not have any line on the lumen. Thus, no accumulation of lipids was detected. The histological image (*f*) illustrates a homogeneous Fibrotic plaque.

2.4 Discussion

Visual plaque characterization requires trained experts, and is complicated by variation in the tissue attenuation and speckle effects. Moreover, large data sets, consisting of hundreds of B-scans, make visual plaque classification impractical, especially in a clinical setting. Therefore, the proposed automatic algorithm could offer an improved plaque classification by analyzing entire pullbacks and assist in clinical diagnosis and therapy guidance.

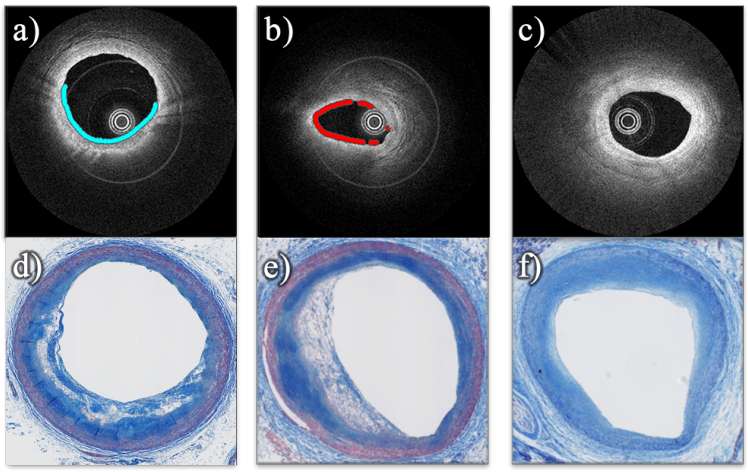

Figure 2.12: Automatic sample level classification. IV-OCT images (first row) with a plot on the section of lumen and the corresponding histological images (second row); where (a) and (b) presenting Lipid plaque, and (c) without lipids.

Methods for texture-based plaque characterization automatically classify each pixel with intensity and texture features, which tend to mislead the correct identification of some pixels where the speckle and attenuation effect is high. On the other hand, methods correlating the backscattering and attenuation coefficients tend to misclassify mixed fibrolipid plaques. Also, the classification using these coefficients can be misinterpreted due to a lack of tissue heterogeneity and intensity calibration.

This work shows that our automated classification method can effectively identify and label A-line profiles based on morphological features. Using the polar IV-OCT images, each A-line is classified to one of the main types of tissue present in atherosclerotic tissue namely: Intimal-Thickening, Fibrotic, Superficial-Lipid, and Fibrotic-Lipid plaque.

The histological evaluation of many of the plaques of our database showed mixed pathological categories. We focused on the two most prominent histopathological categories per plaque. In all plaques included, these two most prominent histopathological categories were always included among the four categories defined for the automated clas-

sification algorithm. However, we had to exclude a few plaques in which the histology was not clear for identifying the tissue types. In addition, two samples with artifacts produced by blood in the lumen were also excluded, since the resulting blood absorption would produce atypical profiles. In the future, we could try to characterize profiles that would allow identifying the presence of blood clots.

Also, macrophages/foam-cells were co-localized with lipids accumulation, so there were present in our Lipids and Fibro-lipids plaques. Calcification and cholesterol crystals were present in a few samples included in our database, but they were not the predominant histological category. Therefore, the presence of macrophages/foam-cells, calcification and cholesterol crystals did not affect significantly the performance of our classification algorithm, in spite of the fact that we did not consider a specific category for these histopathological features. In the future, we could try to characterize profiles that would allow identifying these other histopathological features.

The detection of superficial lipid, and especially the presence of necrotic cores would be clinically relevant. However, to date, OCT has not been shown to be able to differentiate between these two categories. Although the presented algorithm may be able to be trained to identify these two types, there are not enough examples of these two categories in our data set; a larger and more complete data set would be needed to investigate this aspect.

The algorithm was programmed in MATLAB R2016a and tested in a computer with the following characteristics: Windows 7 Enterprise 64-bit, CPU Intel i7 with 6 cores at 3.2GHz, and 48GB RAM. The average processing time for a dataset with 9 B-scans is $\sim$9.5s, from which the optimization process to calculate the profile and abundances described in section 2.2.2 takes $\sim$9s. The average time of processing one single B-scan is $\sim$1.5s, from which the optimization process takes $\sim$1s. Thus, the convergence time of the optimization process is the bottleneck of the algorithm. It is worth mentioning that the code has not been optimized and a parallelized algorithm could allow high throughput

atherosclerotic plaque characterization.

The high classification accuracy of 88% demonstrates the reliability of this method. Additionally, the high sensitivity and specificity for the detection of Fibrotic, Fibrotic-Lipid, and Superficial-Lipid plaques confirm the ability to detect lipid-containing plaques with high accuracy, and quantify this along the pullback segment. Moreover, the estimation of the abundances may give a quantitative indicator of the contribution of a profile class at each A-line. However, there is still a need for the automatic estimation of the optimal value of the regularization parameters (μ and ρ), which in this case were fixed and manually defined by the user for all datasets. Furthermore, the identification of only two class profiles when more than two classes are present in the sample, causes estimation of a combined profile that contains morphological information of mixed classes, which mislead the classification. Further improvements will focus on automatically identifying more than two class profiles and combine those that belong to the same class. Also, employment of additional morphological features combined with texture features might enhance the accuracy of the proposed method.

In a clinical setting, this algorithm will have to deal with the guide wire signal and its shadow, which was not considered in this study. This issue could be resolved by adding a third profile, N=3, to identify the guide wire features reliably. Also, other image processing approaches could be used to identify the guide wire, such as standard deviation filtering or image convolution. Moreover, since the lumen surface is flattened by the elastic transformation method, the distance from the ball-lens to the lumen surface varies between A-lines. This effect might induce signal fluctuations in the A-lines intensities. However, the attenuation by the light propagation from the ball-lens to the lumen surface will be minimal with respect to the tissue effect. Furthermore, these signal fluctuations have minor effect since the profiles are normalized during the synthesis scheme, and the classification depends on the morphology neglecting the amplitude of the profiles.

2.5 Conclusion

In summary, we have presented a novel computational method for automated tissue characterization of atherosclerotic plaques imaged with IV-OCT. This method is based on the modeling of each A-line of an IV-OCT data set as a linear combination of N depth profiles. The profiles are estimated by an alternating least square optimization strategy for an entire pullback segment, and are further automatically classified to a predefined tissue type. In this study, our proposed method was applied to classify each A-line on an IV-OCT B-scan as Intimal-Thickening, Fibrotic, Fibro-Lipid, or Superficial-Lipid. Such profile classification also allowed the automated classification of IV-OCT B-scans as either Lipid-containing or No-Lipid plaques (overall accuracy of $\sim$85%, compared to $\sim$80% based on visual interpretation by a trained IV-OCT reader). Our encouraging results validated on ex-vivo IV-OCT suggest that this methodology has the potential to allow high throughput atherosclerotic plaque assessment through automated tissue characterization.

3. AUTOMATED IDENTIFICATION OF MACROPHAGES/FOAM CELLS CLUSTERS IN INTRAVASCULAR OCT IMAGING

3.1 Introduction

Plaque vulnerability can be defined as the immediate risk of rupture. Rupture-prone plaques represent the majority of vulnerable plaques and show increased presence of inflammatory cells and lipid infiltration with thin-cap fibroatheromas (TCFAs) [30]. Monocytes infiltrate the intima and develop characteristics of macrophages, which can replicate when activated, until eventually become lipid-laden macrophages known as foam cells [31, 32]. Thus, high accumulation of activated macrophages is an important marker in plaque vulnerability along with a thin overlying cap, $< 65\mu$m in thickness, and a large necrotic core that well characterize ruptured plaques [34]. A quantitative comparison of the size of the necrotic core, fibrous cap thickness, macrophage infiltration, in plaque rupture and stable plaques showed that rupture plaques present the highest percent of necrotic core, the shortest fibrous cap thickness, and the highest percentage of macrophages compared to stable plaques [1].

The potential use of OCT imaging for identifying macrophages in atherosclerotic plaques was first investigated by statistical correlation of the normalized standard deviation (NSD) from selected regions in OCT scans and corresponding histological CD68 images [35]. In that study, the NSD was estimated from the pixel values of a defined region of interest (ROI) as follows:

$$NSD = \frac{\sigma}{S_{max} - S_{min}} \tag{3.1}$$

and

$$\sigma^2 = \frac{1}{N-1} \sum ROI_{width} \sum ROI_{height} \left(S(x,y) - \bar{S}\right)^2 \tag{3.2}$$

where N is the total number of pixels in the ROI, and $S(x,y)$ is the OCT signal as a function of x and y locations within the ROI. This study demonstrated the ability of OCT imaging of visualizing and quantifying macrophages in a fibroatheroma. Other study analyzed the correlation of clinical syndrome of atherosclerosis with macrophage distributions, where the sites of plaque rupture showed greater both multi-focal and focal macrophage densities than non-ruptured sites [36].

A further first in vivo data study demonstrated the ability of NSD in outlining critical features of plaque vulnerability, where the association of the peripheral white blood cell count and TCFA macrophage density served as markers of inflammation in vulnerable plaques [37]. Later, an ex vivo study using NSD demonstrated that rupture sites presented significantly higher macrophage density compared to non-ruptured culprit sites [38]. Latterly, a quantitative algorithm was employed to identify bright spots in intravascular OCT images, which confirm that bright spots are not only caused by macrophages (57% of bright-spot positive regions) but also by combination of other plaque components that create abrupt changes in the refractive index [39]. The reported overall sensitivity of this method was 80%, yet the specificity was only 49% since this algorithm is prone to detect other sources of bright spots not belonging to macrophages. Recently, a new study compared the potential of NSD, signal attenuation, and granulometry index of identifying the macrophage presence in ex vivo OCT imaging of 15 coronary arteries, where the NSD showed the highest accuracy of 90% [40]. However, the OCT images were obtained from formalin-fixed samples, which might have affected the OCT signal.

As stated by the IV-OCT consensus [6], the main characteristics of macrophage accumulations in IV-OCT images are as follows:

- Macrophages produce signal-rich regions with punctuated bright spots that exceed the intensity of background speckle noise
- Macrophages can only be assessed in the context of a fibroatheroma
- Macrophages are localized between the bottom of the cap and the top of a necrotic core
- The IV-OCT signal is significantly attenuated shadowing the underlying tissue
- Microcalcifications, cholesterol crystals, or internal/external elastic membrane can be confused with macrophages accumulation
- The detection of macrophages require high axial and lateral resolutions in IV-OCT

Based on these characteristics, the methodology presented here proposes an algorithm for automatic identification of significant macrophages accumulation in IV-OCT images and it is not restricted to the fibrous cap but it can also interrogate the whole plaque area.

3.2 Methods

The proposed approach is based on the OCT-NSD (raw signal) analysis presented in [35, 37, 38] and has been designed to improve both the sensitivity and the specificity of the detection of macrophage/foam cells (M/FC) clusters. Following the macrophage characteristics defined in section 3.1, this methodology intends to identify punctuated signal-rich regions with high NSD followed by high signal attenuation, or shadows, in the subsequently deeper axial region, which would result in a more accurate identification of M/FC clusters discriminating areas with high NSD without M/FC presence. Furthermore, this method is not restricted to the NSD and may use any other texture granularity features, such as the entropy that is likewise analyzed here. To achieve this, the NSDRatio concept is introduced where two square ROIs of same size are defined for a normalized standard

deviation moving filter: a main area (ROI1), centered at bright spots where M/FC are expected, and a subsequent deeper region (ROI2) with high signal attenuation. Thus, regions with bright spots (having high normalized standard deviation) followed by a highly attenuated signal region (lower normalized standard deviation) in the axial direction will present elevated NSDRatio values, which would be characteristic of macrophage clusters. Figure 3.1 displays the two regions superimposed on the OCT image with their centers separated by certain distance or span. The arrangement of these ROIs is intended to discriminate other regions producing high NSD and lacking of M/FC. The NSDRatio is simply defined as:

$$NSDRatio = \frac{NSD_{ROI1}}{NSD_{ROI2}} \tag{3.3}$$

This work focuses in analyzing the advantage of the NSDRatio over the NSD, however, the entropy is also proposed as a potential feature. Therefore, the Entropy Ratio can be similarly defined as:

$$ENTRatio = \frac{ENT_{ROI1}}{ENT_{ROI2}} \tag{3.4}$$

where

$$ENT_{ROI} = -\sum ROI_{width} \sum ROI_{height} \left[S(x,y) Log_2 \left(S(x,y)\right)\right] \tag{3.5}$$

Since the entropy may give zero for regions with minimum values (brackground signal), it is shifted by one unit ($ENT_{ROI} + 1$) to avoid zero division.

Figure 3.2 summarizes the process of computing the or ENTRatio of an IV-OCT image. The catheter ball lens and sheath signal produce bright lines, which are removed together with the lumen signal. The polar OCT (raw) image is normalized from 0 to 1 by dividing each pixel by the difference between the maximum and minimum value in the image. The filtered image is calculated for each pixel with a moving filter (standard deviation or entropy) as defined in equations (3.3) and (3.4) and the ratio is calculated by dividing

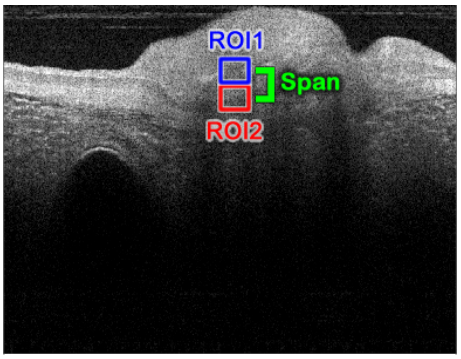

Figure 3.1: OCT image with overlaid main ROI (ROI1, blue) and preceding ROI (ROI2, red) used to estimate the NSDRatio and ENTRatio.

the resulting filtered image by its own copy with its elements shifted a predefined number of pixels, or span, in the axial direction. A binary circular kernel is employed for the texture filter to ignore those pixels far form the central point of the window, yet a squared or even a weighted Gaussian kernel can be used. A binary mask, defined by the Otsu's method [41, 14] and morphological operations, is applied to the resulting image to remove components coming from elements not belonging to the plaque, such as the media and the adventitia layers. A threshold is utilized for binary classification to separate the regions with M/FC clusters. Finally, the detected pixels with high ratio values (above a pre-defined threshold) are overlaid on the log compressed IV-OCT for image display.

3.3 Database

A set of IV-OCT images were acquired from cadaveric human coronary arteries using a fiber-based intravascular PS-OFDI system [3, 29]. This system has a swept range of 115 nm, centered at 1320 nm, and a repetition rate of 54 kHz. This system is a polarized sensitive OCT, which measures two orthogonal polarization channels in parallel and alternates the polarization state of the light incident on the sample in between A-lines. However, the method was applied to the sum of the squared norm of the complex-valued tomogram of

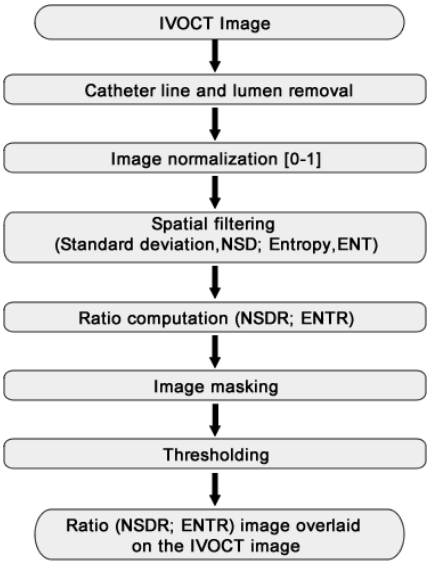

Figure 3.2: Block diagram and sequence of the automatic M/FC identification process.

each channel ignoring the modulation of the polarization states in between A-lines. The database consists of 28 data sets of IV-OCT images. Each data set was formed by 9 consecutive frames, spaced by 100 μm, of 1024 depth-pixels with an axial resolution of 4.8 μm, assuming the tissue refractive index of 1.34, and 1024 A-lines with an angular sampling step of $0.35°$. The central frame (number 5) of each IV-OCT dataset was matched with the histological sections (CD68 and Masson's Trichrome).

3.4 Validation

The NSD, NSDRatio, ENT (Entropy), and ENTRatio images were computed for the central frame (number 5) of each of the 26 IV-OCT datasets. The histopathological evaluation was performed by visually localizing M/FC clusters in the CD68 and Trichrome images, and finding landmarks that help to match the histological images with the OCT image in order to select the indices of the A-lines containing M/FC as the true condition for the classification process. Therefore, each A-line was annotated as having or not M/FC

based on the matched histological evaluation (gold-standard), and an automated classification based on a selected threshold for either the NSD, ENT, NSDRatio or ENTRatio. A total of 15 samples where clearly identified as positive M/FC presence with different degrees of M/FC accumulation and 13 samples without M/FC presence in the the histology-based classification. The classification performance of this method was estimated by Receiver Operating Characteristic (ROC) analysis.

3.5 Results

3.5.1 Filter size determination

The size of the moving window filtered was determined based on the ROC curve of different ROI sizes applied to the 5th frame of the 28 samples. Figure 3.3 shows a comparison of the ROC areas of the NSD, NSDRatio, ENT, and ENTRatio for different ROI sizes; the width, height, and span had the same magnitude showed in the plot X-axis. An ROC area closer to one indicates superior classification performance. The NSD and ENT had significantly lower area values compared to the NSDRatio and ENTRatio; the ENTRatio produced slightly higher area values.

The larger the ROI size the higher the computational cost of the moving window filter. Therefore, since there is no significant improvement in performance (ROC area) after a magnitude of 55 pixels, the selected optimum ROI size was $[55 \times 55]$ pixels or $[264 \times 264]\mu$m (see Fig. 3.3).

3.5.2 Thresholding and depth level analysis

The classification threshold was likewise determined by the analysis of ROC curves from different depth levels. This analysis shows the effectiveness of this approach in identifying not only superficial but also deeper M/FC clusters at different axial depths. Figure 3.4 shows plots of the ROC curves at different maximum interrogation depths for the NSD, ENT, NSDRatio, and ENTRatio.

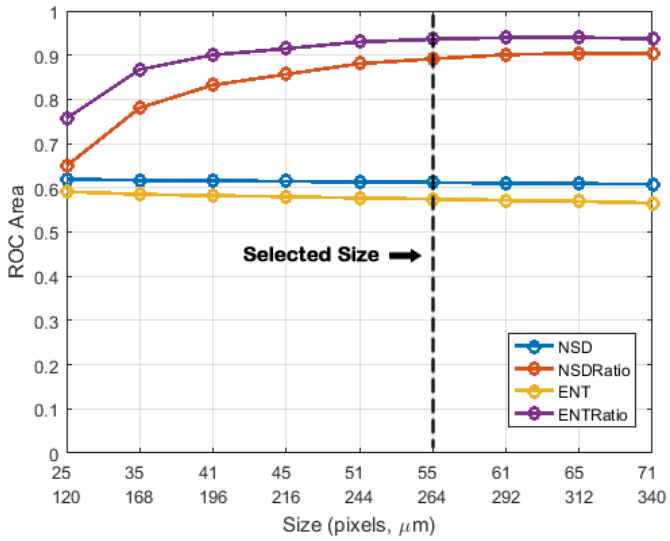

Figure 3.3: ROC area comparison of the NSD, NSDRatio, ENT, and ENTRatio for different ROI sizes. The window width, height, and span were set to the same magnitude showed in the X-axis; the X-axis labels show the odd size in pixels (top) and micrometers (bottom).

The NSD and ENT led to very similar low ROC area values (poor performance) at all the depth levels with a highest ROC area at 500 μm. In contrast, the NSDRatio and ENTRatio ROC areas increased with respect of the depth having the highest ROC area at 700 μm. This is also illustrated in Fig. 3.5. Notice that the performance of the ENTRatio remains almost the same after 700 μm, so it can probe deeper into the plaque without compromising detection accuracy. The NSDRatio, on the other hand, shows slightly lower performance beyond 700 μm.

Based on the ROC analysis, the NSD had a low accuracy of 55.6% with a sensitivity of 56.6% and a specificity of 55.3% for the classification of the 28 samples. On the other hand, the NSDRatio showed an accuracy of 86% and a sensitivity and specificity of 85.8% and 86.1%, respectively. Similarly, the ENTRatio led to an accuracy of 86.9% and a sensitivity and specificity of 86.8% and 86.9%, respectively.

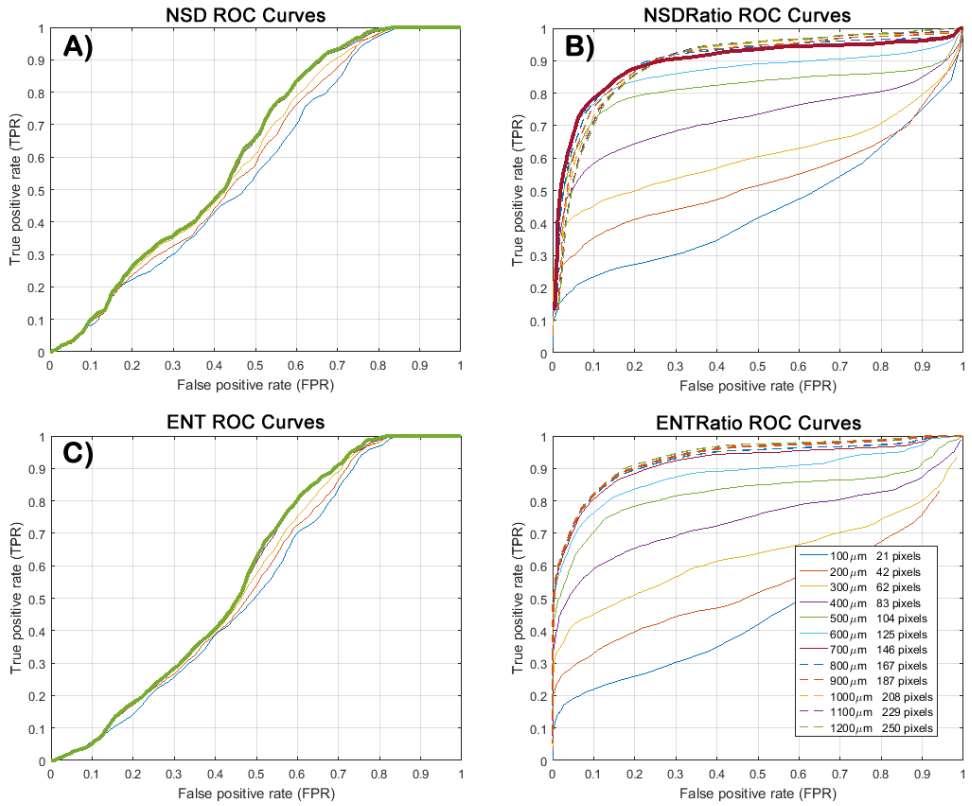

Figure 3.4: Plots of ROC areas of the NSD (A), NSDRatio (B), ENT (C), and ENTRatio (D) at different depth levels ranging from 100 μm to 1200 μm.

In terms of speed of the moving window filter, the normalized standard deviation takes about 0.35 s to process one frame (1024×1024 pixels) while the entropy takes approximately 11.5 s using the standard functions of MATLAB R2016a running on a computer with Windows 7 Enterprise 64-bit, CPU Intel i7 with 6 cores at 3.2 GHz, and 48 GB RAM. Thus, the NSDRatio is considerable faster, $32.6\times$, than the ENTRatio. However, the ENTRatio images have less variability as a function of depth as illustrated in Figs. 3.4 and 3.5.

Since this approach is based on a binary classification, a discrimination threshold was selected from the ROC curve with the maximum area of each method. In this way, the thresholds for NSD and ENT were selected as 0.02 and 4.78 a.u., respectively, while the

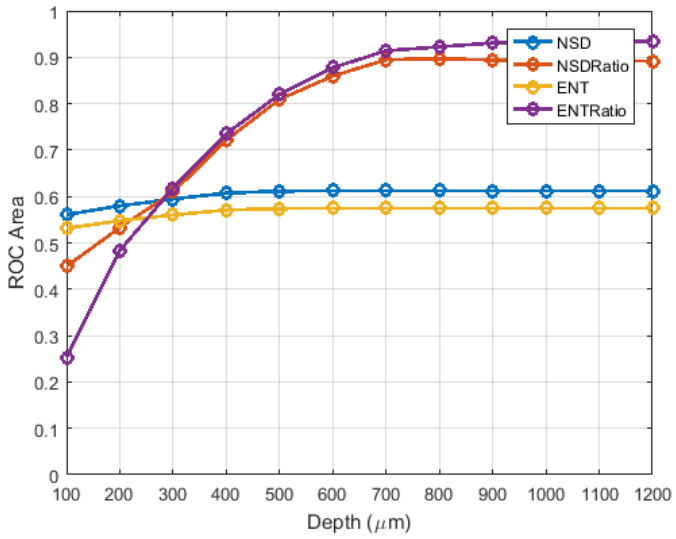

Figure 3.5: Comparison of ROC areas of the NSD, NSDRatio, ENT, and ENTRatio at different depth levels ranging from 100 μm to 1200 μm.

thresholds for NSDRatio and ENTRatio were 13.75 and 2.44 folds (These units are expressed in folds of the ROI1 with respect of the ROI2), respectively.

3.5.3 Linear correlation analysis

A linear correlation analysis was performed to find the linear dependence of the percentages of detected M/FC between the histology-based and the automated classification of the four texture features using the aforementioned selected thresholds. Figure 3.6 shows scatterplots of the data patterns produced by the linear correlation; each plot with its corresponding R and P values for a 95% confidence.

The correlation plot between histology-based and the NSD classification in Fig 3.6(A) shows a weak linear correlation with a random pattern of scattered points, which is confirmed by a low value of $R = 0.19$ and $P > 0.05$. Likewise, the correlation between histology-based and the ENT classification, Fig 3.6(C), exhibits a weak linear correlation $R = 0.12$. In contrast, as depicted in Fig 3.6(B), the data points fall close to a straight line,

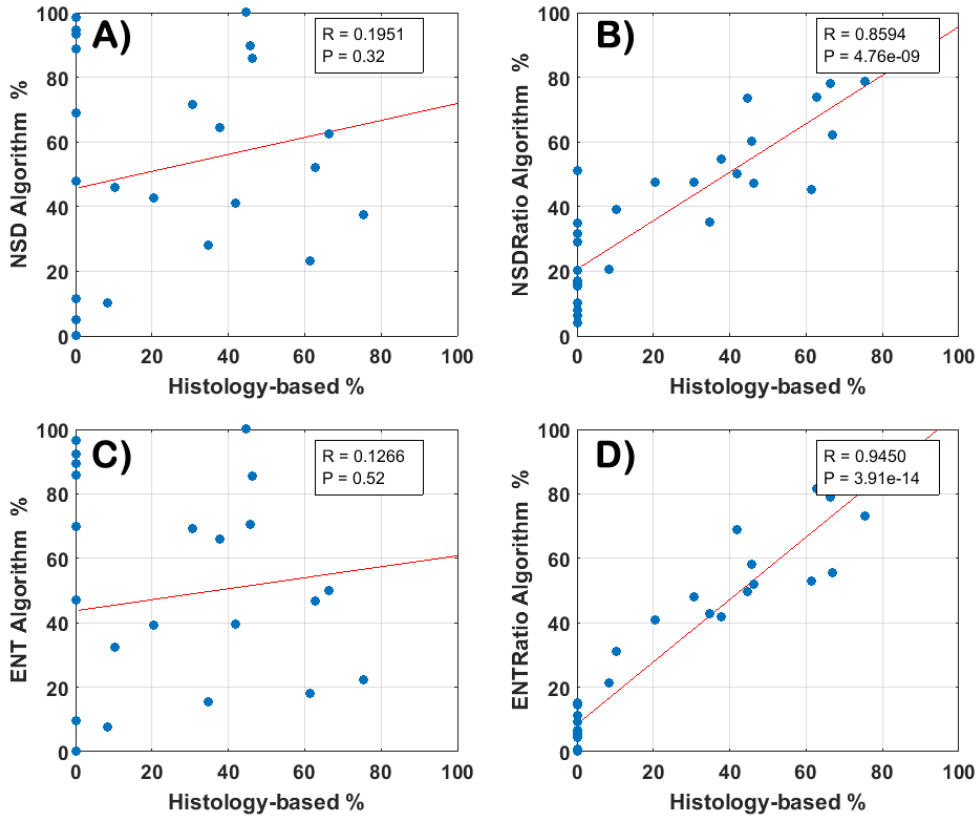

Figure 3.6: Linear correlation plots of the percentages of detected M/FC between the histology-based and the automated classification of the four proposed texture features: NSD (A), NSDRatio (B), ENT (D), and ENTRatio (C); R and P values for a 95% confidence.

which indicates that the NSDRatio and the histology-based classification have stronger linear relationship with a high value of $R = 0.85$ with $P < 0.05$. Similarly, the high value of $R = 0.94$ for the correlation between the ENTRatio and the histology-based classification validates a strong linear correlation. Thus, the NSDRatio, and ENTRatio are strongly correlated with the histopathological evaluation and have the potential of classifying M/FC clusters with high accuracy.

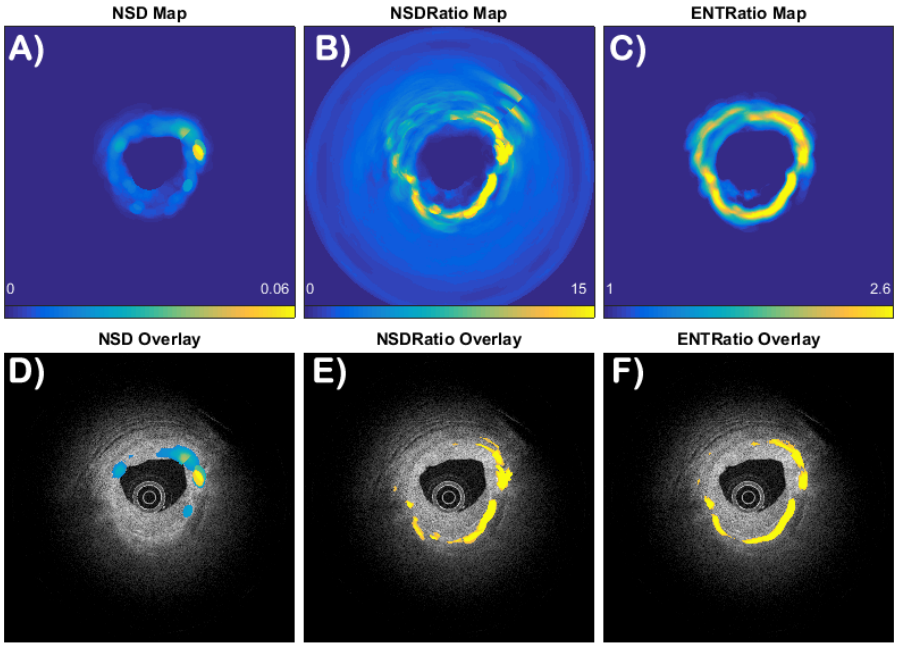

Figure 3.7: Texture maps and overlaid images. NSD (A), NSDRatio (B), and ENTRatio maps (C). IV-OCT image with the NSD (D), NSDRatio (E), and ENTRatio (F) images overlaid.

3.5.4 Classification

Each B-scan is processed following the procedure in Fig. 3.2 to compute color-coded texture maps and to show the map overlaid on the B-scan. Figure 3.7 shows an example of the resulting NSD, NSDRatio, and ENTRatio maps (first row) and the IV-OCT image with the texture maps overlaid (second row); the colored highlighted regions in the overlaid image are the pixels that overpassed the selected threshold.

The algorithm automatically classifies each A-line as positive or negative for M/FC presence if at least 10 pixels have an index value above the corresponding threshold. Figure 3.8 shows the histological images, the histology-based classification marking the positive A-lines with arcs, and the automatic classification result of the NSD, NSDRatio, and ENTRatio for a sample with different degrees of M/FC accumulation. As shown in the

histological images (A and B), there are superficial (white arrows), and deeper (red arrows) M/FC clusters and scattered M/FC (yellow arrows). In this particular case, the three methods were able of identifying those areas marked as positive for M/FC presence, however, the NSD highlighted regions where no M/FC where found in the histological image (cyan arrow in D). The NSDRatio and ENTRatio missed part of a deep M/FC cluster (blue arrows). Although scattered M/FC were not considered in the histology-based classification, the ratio approaches were able of identifying those areas (yellow arrows in E and F).

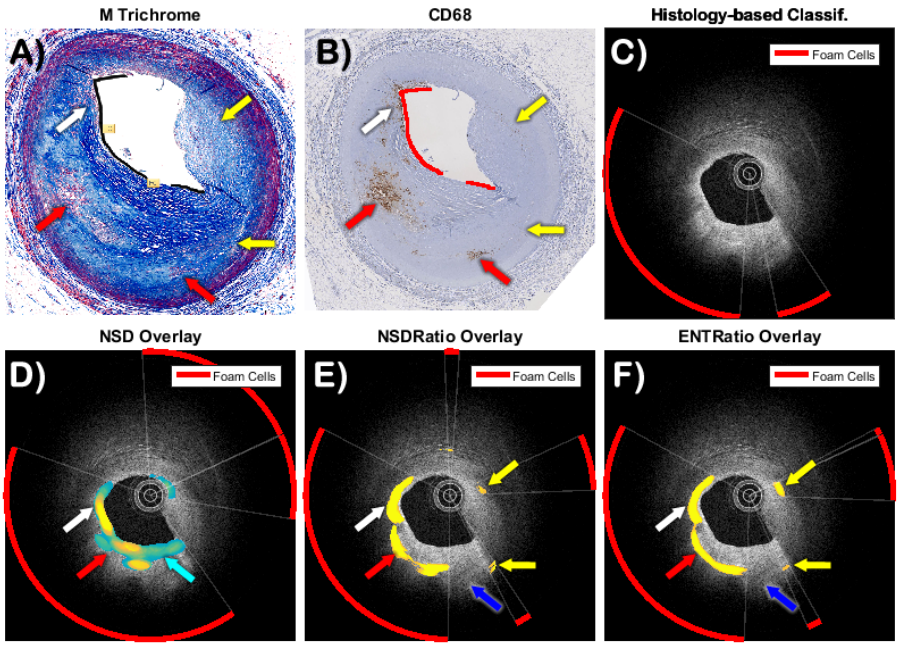

Figure 3.8: Classification result of the NSD, NSDRatio, and ENTRatio for a sample with superficial (white arrows) and deeper (red arrows) M/FC accumulation, and scattered M/FC (yellow arrows); Histological images Masson's Trichrome (A) and CD68 (B); histology-based classification (C); IV-OCT image with the NSD (D), NSDRatio (E), and ENTRatio (F) maps overlaid, respectively; the arcs on the IV-OCT image mark those section of the artery with M/FC. The NSD tends to highlight areas (cyan arrow in D) where no M/FC where found in the histological image while the NSDRatio, and ENTRatio missed part of a deep M/FC cluster (blue arrows). The NSDRatio, and ENTRatio are able to identify scattered M/FC (yellow arrows).

The sample in Fig. 3.9 presents high concentration of M/FC between the fibrous cap and the top of the necrotic core. In this case, the NSD had elevated values for areas with intimal thickening and for a small region where the M/FC were localized and missed part of the overlaying region of the necrotic core (red arrows). On the other hand, the NSDRatio and ENTRatio were able of fully identifying the region of the necrotic core covered by M/FC. However, both the NSDRatio and ENTRatio produced false positives in regions of the adventitia layer due signal fluctuations in the connective tissue.

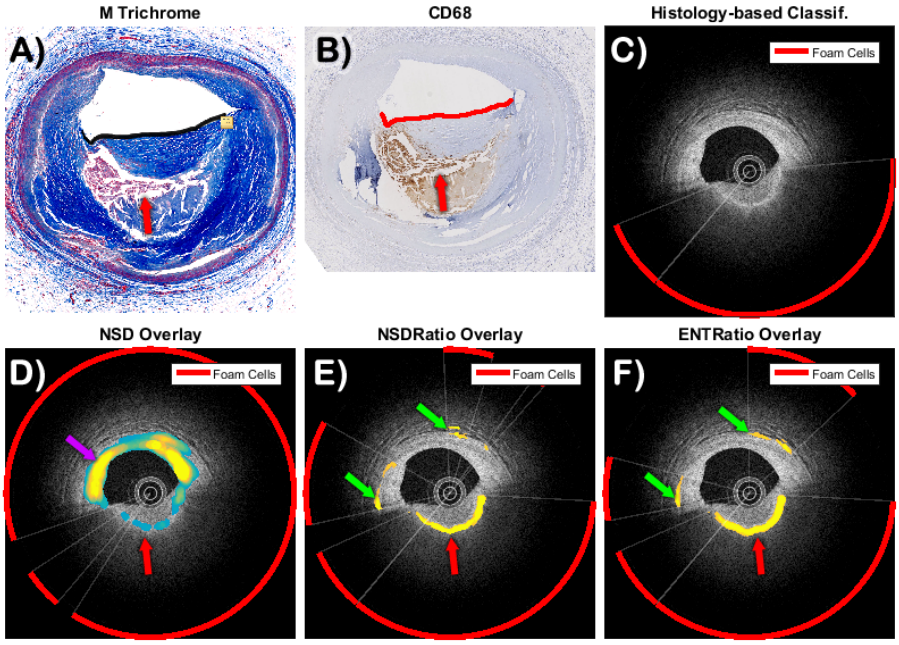

Figure 3.9: Classification result of the NSD, NSDRatio, and ENTRatio for sample with high M/FC accumulation (red arrows) between the overlaying fibrous cap and the necrotic core. A) Masson's Trichrome image; B) CD68 image; C) histology-based classification; D) E) and F) IV-OCT image with the NSD, NSDRatio, and ENTRatio maps overlaid, respectively. The magenta arrow points at a region of false positives in the NSD map. The green arrows show false positives in the NSDRatio and ENTRatio maps.

In the example shown in Fig. 3.10, it is noticeable that the artery has a well-defined

area with M/FC (red arrows) that covers approximately 65% of the lumen artery. The NSD classification highlighted most of the intimal thickening region (magenta arrows) and missed most of the M/FC clusters (red arrows) in spite of the high M/FC density. On the contrary, NSDRatio and ENTRatio were able of identifying more than 90% of the M/FC region. However, as in the previous example where the artery is thin, the NSDRatio and ENTRatio were prone to false positives (green arrows) on areas with high signal from the adventitia layer and signal variations from the connective tissue. Further image processing might help to discriminate these regions.

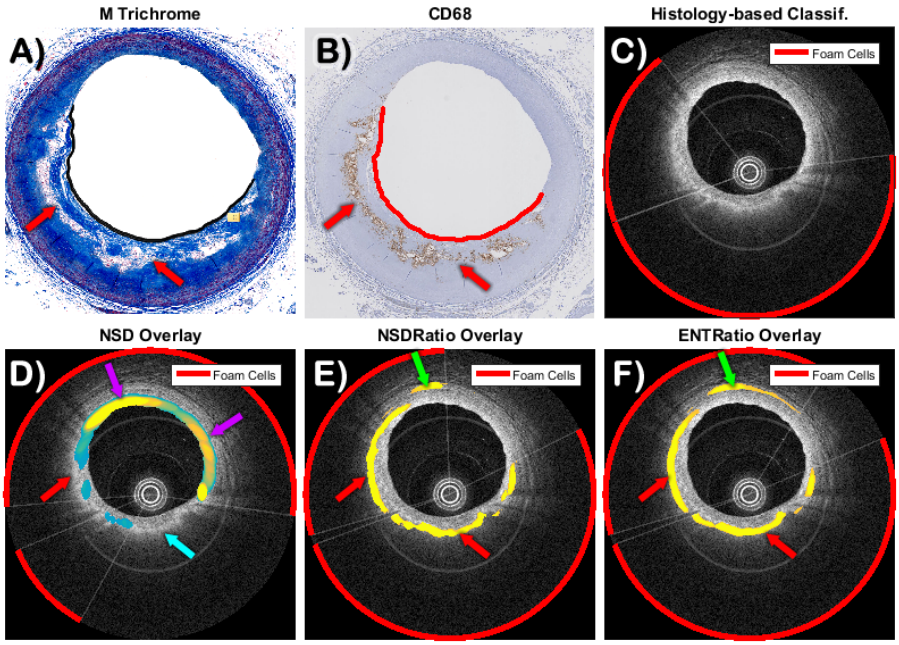

Figure 3.10: Classification result of the NSD, NSDRatio, and ENTRatio for sample high M/FC density (red arrows). A) Masson's Trichrome image; B) CD68 image; C) histology-based classification; D), E) and F) IV-OCT image with the NSD, NSDRatio, and ENTRatio maps overlaid, respectively. The NSD missed half of the region with M/FC (cyan arrow). The NSDRatio and ENTRatio were able of identifying all the area marked with M/FC, however, there are false positives (green arrows in E) and F)) produced by the high signal from the adventitia and the signal fluctuations in the connective tissue.

In the last example shown in Fig. 3.11, the artery was classified as negative for M/FC presence. In this case, the three methods classified the sample as no M/FC detected. As in the previous examples where the artery is thin, the NSDRatio and ENTRatio are prone to false positives (cyan arrows) on areas with high signal from the adventitia layer and signal variations from the connective tissue.

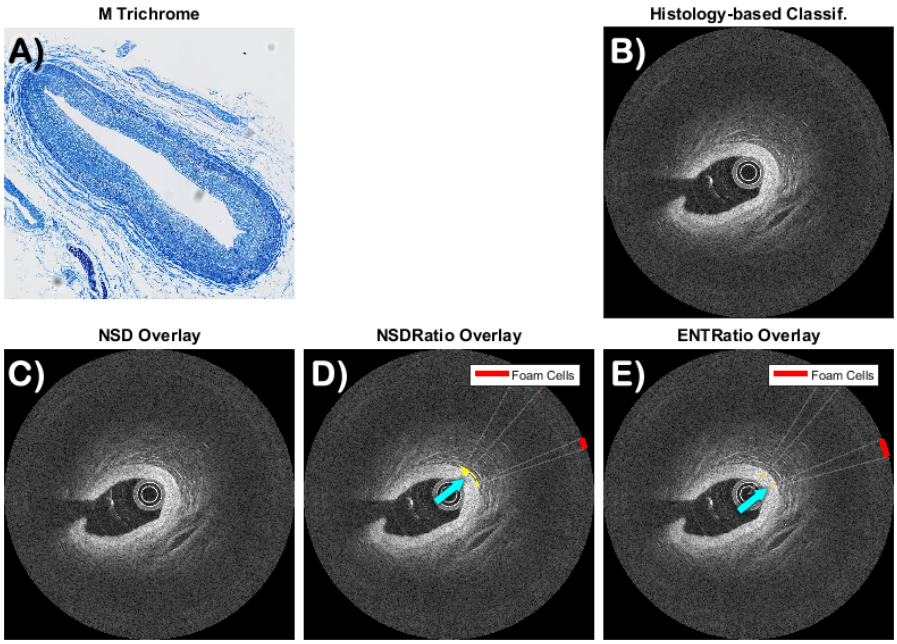

Figure 3.11: Classification result of the NSD, NSDRatio, and ENTRatio for sample without M/FC presence. A) Histological image; B) IV-OCT Reader classification; C), D), and E) IV-OCT image with the NSD, NSDRatio, and ENTRatio images overlaid, respectively; the cyan arrows point at false positives.

3.6 Discussion

The NSD approach provides a method to identify areas with macrophages. However, other types of tissue produce high NSD values leading to misclassification giving low ROC area values as it was illustrated in Fig. 3.3. On the other hand, NSDRatio and ENTRatio

provide a more reliable way of identifying agglomeration of M/FC in IV-OCT images leading to significantly higher ROC area values than the NSD. The high signal from the adventitia layer and signal variations from the connective tissue lead to high ratio values. Although these false positives reduce the specificity, these regions are located outside the intima layer. Further image processing for removing those false positives will improve the accuracy of the proposed approach. Since the threshold is selected using ROC curves, the selection of the best threshold can be biased to increase either the sensitivity or the specificity.

3.7 Conclusions

In summary, our results show that the proposed NSDRatio and ENTRatio increase the sensitivity and specificity of the identification of M/FC clusters compared to the NSD, which may help to reveal plaque vulnerability. Using the ROC analysis, the NSD showed a classification accuracy of 55.6% while the NSDRatio and ENTRatio showed accuracies of 86% and 86.9%, respectively. Therefore, the radio concept introduced here may be used to discriminate other regions producing high NSD and lacking of M/FC. The NSDRatio and ENTRatio have low complexity and computational cost, so they can be implemented for in vivo discrimination of vulnerable plaques.

4. AUTOMATIC DETECTION OF MACROPHAGES/FOAM CELLS IN OCT-FLIM IMAGES OF HUMAN ATHEROSCLEROTIC PLAQUES

Plaque vulnerability can be defined as the immediate risk of plaque rupture, which is the main cause for the majority of acute coronary syndromes. Vulnerable plaques show increased presence of inflammatory cells and lipid infiltration with thin-cap fibroatheromas (TCFAs) [30]. Monocytes infiltrate the intima and develop characteristics of macrophages, which can replicate when activated, until eventually become lipid-laden macrophages known as foam cells [30, 31, 32, 33]. The culprit lesions include numerous macrophages and rare smooth muscle cells. Ruptured plaques present lesions with a necrotic core, an overlying thin fibrous cap, < 65 μm in thickness, and high macrophage infiltration [34]. The relationship between the macrophage density and the fibrous cap thickness has been demonstrated; the higher the macrophage density, the thinner the fibrous cap [42]. Thus, the fibrous cap thickness depends on the extent of macrophage infiltration. Consequently, the density of macrophage clusters in atherosclerotic plaques can be used as a predictor of plaque vulnerability.

Several studies have used OCT to evaluate the thickness of the fibrous cap and its potential use in assessing plaque vulnerability [7, 43, 44]. A quantitative analysis showed the relationship between the size of the necrotic core, the fibrous cap thickness, and the macrophage infiltration in ruptured and stable plaques [1]. That study demonstrated that, compared to stable plaques, ruptured plaques contain higher percentages of necrotic core, shorter fibrous cap thickness, and higher percentages of macrophages.

The first study that showed the ability of OCT to quantify macrophage density in atherosclerotic plaques made use of the NSD [35]. The NSD was measured form a defined region of interest to prove that the OCT signal variance and the presence of macrophages

in CD68 histological images are correlated. The NSD was defined as follows:

$$NSD = \frac{\sigma}{S_{max} - S_{min}} \tag{4.1}$$

and

$$\sigma^2 = \frac{1}{N-1} \sum ROI_{width} \sum ROI_{height} \left(S(x,y) - \bar{S}\right)^2 \tag{4.2}$$

where N is the total number of pixels and $S(x,y)$ is the OCT signal as a function of x and y locations within the ROI. Further studies have demonstrated the ability of OCT imaging to estimate macrophage concentration using the NSD [36, 37, 38, 40, 39].

The main characteristics of macrophage agglomerations described in the IV-OCT consensus [6] are summarized as follows:

- Macrophages produce signal-rich regions with punctuated bright spots that exceed the intensity of background speckle noise.
- Macrophages can only be assessed in the context of a fibroatheroma.
- Macrophages are localized between the bottom of the cap and the top of a necrotic core.
- The IV-OCT signal is significantly attenuated, shadowing the underlying tissue.
- Microcalcifications, cholesterol crystals, or internal/external elastic membranes can be confused with macrophage accumulation.
- The detection of macrophages requires high axial and lateral resolutions in IV-OCT.

Although little is known about the relationship between autofluorescence and macrophage infiltration in fibroatheromas, studies have shown that endogenous fluorescence can be

used to assess macrophage presence in atherosclerotic plaques [45]. Time-resolved fluorescence spectroscopy,which measures spectral intensity and average lifetime of three channels (390, 430 and 470 nm), was investigated for diagnosis of unstable atherosclerotic lesions in human coronary artery [46]. Variations in fluorescence lifetime values are strongly associated to the content of collagen, lipids, and macrophages in atherosclerotic plaques [47, 48, 49]. In another study, a nitrogen pulse laser (337 nm, 1 ns) was used to induce tissue autofluorescence, in a rabbit model of atherosclerosis, that was collected at three emission wavelengths (390, 450, and 500 nm) [47]. A stepwise linear discriminant analysis algorithm used parameters derived from the emission for classification.

Similarly, further studies of human carotid plaques that induced autofluorescence by a 337 nm laser allowed the use of intensities, lifetimes, and Laguerre expansion coefficients of three spectral bands (440, 380, and 550 nm) as markers of plaque vulnerability [48, 50]. Later, Phipps showed that although macrophages do not fluoresce by themselves, foam cells exhibit short average fluorescence lifetimes according to their lipid content [51]. That study demonstrated the potential of FLIM imaging of human coronary arteries to discriminate macrophage-rich areas. Another work validated the ability of FLIM to detect macrophages in fibrous caps with high sensitivity, complementing the commonly used intravascular ultrasound (IVUS) imaging for the assessment of human coronary arteries [52].

Lately, multimodal imaging systems have emerged as robust methods for the characterization of atherosclerotic plaques. A catheter-based multimodal OCT and near-infrared autofluorescence (NIRAF) intravascular imaging system was employed for in vivo imaging of human coronary arteries [53]. In that study, OCT was able to provide structural images at a microscopic level and NIRAF exhibited elevated autofluorescence in necrotic core lesions. Raman spectroscopy, in combination with FLIM, has been used to characterize human coronary specimens using a bimodal probe, in which FLIM provides infor-

mation from the fibrous cap, while Raman's higher penetration depth helps to distinguish lipids from necrotic cores [54].

Our group has demonstrated the ability of multispectral FLIM to characterize the biochemical content of human coronary atherosclerotic plaques [55]. The sample was excited using a pulsed UV laser (337 nm), and the emission was collected at three emission bands (390 ± 40 nm, 450 ± 40 nm, and 550 ± 88 nm) for the purpose of distinguishing elastin-dominant plaques (peak emission at 450 nm, 1.5 ns lifetimes) from collagen-dominant plaques (peak emission at 390 nm, 2-3 ns lifetimes) based on their intrinsic fluorescence spectral and lifetime differences. Also, multispectral FLIM was combined with OCT to simultaneously characterize the 3D morphology and biochemical composition of ex vivo human atherosclerotic artery tissue and in vivo cancerous hamster cheek pouch [57, 58]. These findings were later corroborated by two different automated classification approaches with high sensitivity and specificity using intensities and lifetimes from the spectral channels and validated by histopathology [59, 60].

4.1 Methods

The approach presented in this work makes use of multimodal OCT-FLIM images of postmortem coronary arteries; the OCT-FLIM system used for this study was previously described in [61]. The OCT system has a swept range of 100 nm, centered at 1310 nm and a repetition rate of 50 kHz, with lateral and axial resolutions of 34 μm and 7 μm, respectively. A Mach-Zehnder type interferometer (MZI) provided a wavelength reference for spectral calibration and linearization. The excitation source for the FLIM system was a frequency tripled Q-switched Nd:YAG at 355 nm pulsed at 10 kHz with a width of 2 ns and a maximum energy of 5 μJ. The fluorescence emission was separated into two spectral channels by combinations of dichroic mirrors and bandpass filters: 390 ± 20 nm for channel 1, and 494 ± 20.5 nm for channel 2. The time-resolved fluorescence emissions

were collimated into two multimode fibers with different lengths of 1 m and 11.5 m to provide a separation time of $\sim$ 60 ns between channel1 and channel 2. Then, a multi-channel plate photomultiplier tube with 150 ps rise time collected the fluorescence. The lateral resolution for FLIM was 120 μm. The combined system field of view was 16×16 mm. The OCT imaging produces volumetric images while FLIM creates 2D maps.

4.1.1 OCT macrophage identification

The proposed identification of macrophages in OCT images relies on the OCT-NSD approach previously established [35, 37, 38] with a variation to improve the sensitivity of the detection of agglomerated macrophage/foam cells.The idea behind this method is to identify punctuated signal-rich regions with high NSD followed by high signal attenuation in the subsequently deeper axial region. This could characterize the effect of M/FC clusters in OCT images by calculating the ratio between these two regions. To accom-

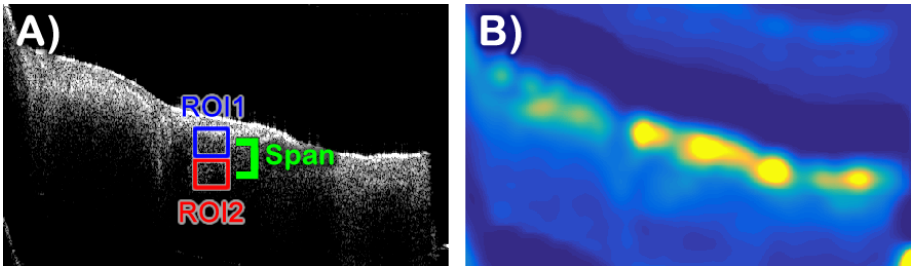

Figure 4.1: A) OCT image with overlaid main ROI (ROI1, blue) and preceding ROI (ROI2, red) used to estimate the NSD-Ratio. B) NSD-Ratio mapcalculated from image A), highlighting areas with high macrophage density.

plish this, two square ROIs of the same size separated by certain distance or span (see Fig. 4.1(A)) are defined for the computation of the NSD-Ratio. The ROI1, or main area, is centered where the bright spots produced by M/FC are anticipated, the ROI2 is located in a subsequent deeper region with expected high signal attenuation. The NSD-Ratio is

pixel-wise calculated to form a map from the B-scan. Hence, the NSD map, Fig. 4.1(B), for the ROI1 is computed using a standard deviation moving filter with a circular kernel of diameter equal to the size defined for the ROIs. The NSD of the ROI2 is simply a copy of the NSD of the ROI1 with its elements shifted a predefined number of pixels in the axial direction. The NSD-Ratio is defined as:

$$NSDRatio = \frac{NSD_{ROI1}}{NSD_{ROI2}} \tag{4.3}$$

4.1.2 FLIM macrophage identification

The FLIM images are computed from time resolved fluorescence measurements using an iterative nonlinear least squares biexponential model [56]. The collected signal of each channel is deconvolved with the measured instrument response corresponding to each channel. The absolute intensity is computed by dividing the fluorescence decay acquired from each channel by integrating the fluorescence decay from both channels. The average florescence lifetime is calculated using the deconvolved temporal signal decay at each spatial position [57]. For each channel, pairs of 2-D normalized intensity and lifetime maps are formed, see Fig. 4.2.

The proposed identification of macrophages in FLIM images is based on a threshold applied to the lifetime map formed from the fluorescence decay of the second channel (494 nm). The optimum threshold is selected using the receiver operating characteristic analysis by comparing the histology-based (gold standard) classification against the outcome of the automatic classification for different thresholds.

4.2 Database

OCT-FLIM images of cadaveric human arteries were acquired with a multimodal system previously described [61]. The database consists of OCT-FLIM images of 7 artery

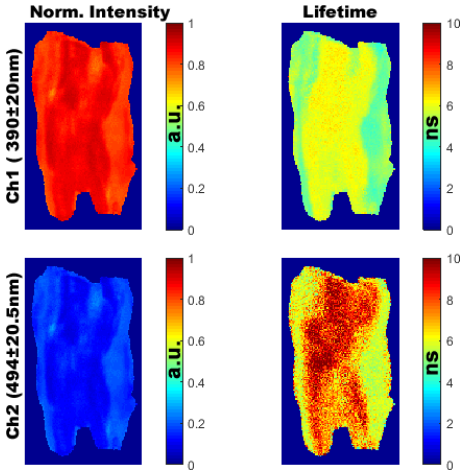

Figure 4.2: FLIM images of the first (390 nm) and second (494 nm) channels of a coronary artery segment. Normalized intensity (left) and lifetime map (right).

segments with their corresponding histological slices (3 or more histology cuts per segment) stained with CD68. The histology slices were cut from specific points previously inked on the right side of the artery lumen (see Fig. 4.3(A)) to be able of matching the histology and the OCF-FLIM images. The top of the artery was also inked and a small notch was made in the bottom to help find the correct orientation. Each dot corresponds to a specific row index in the FLIM images (magenta line in Fig. 4.3(B)), a B-scan index from the OCT volume (magenta line in Fig. 4.3(C)), and the corresponding CD68 histology slice (Fig. 4.3(D)).

4.3 Validation

Each slice from the histological image was visually evaluated for the existence of macrophages. For each slice, segments of the surface lumen were marked as either positive or negative for macrophage presence within 200 μm from the lumen using Aperio ImageScope (Leica Biosystems) histology software. The lengths of these segments were converted to proportions by dividing each segment by the total length of the lumen. These proportions were used to match the indices of the A-lines and the indices of FLIM pix-

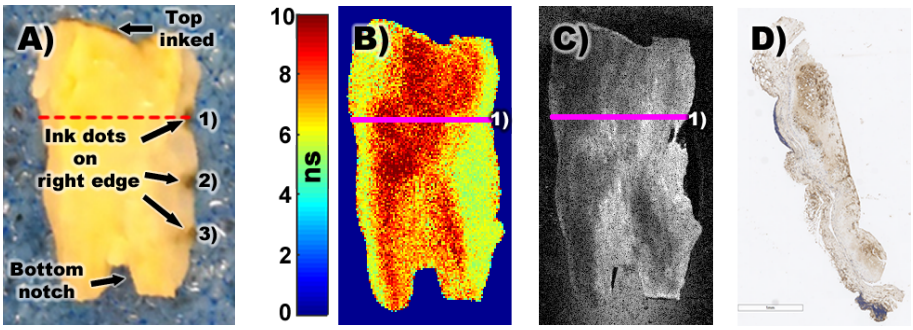

Figure 4.3: Artery inking procedure and correlation to the FLIM and OCT images. A) Raw picture of the artery with the inked dots at the right side, the top part inked, and a bottom notch for orientation. The red dotted line is an estimation of where the slice was cut for histology. B) Lifetime map (0 - 10 ns) of the second channel with a magenta line indicating the correspondence of the row index with the first inked dot on the artery. C) The OCT en face image with a magenta line indicating the index of the B-scan corresponding to the first inked dot. D) The CD68 histological image corresponding to the first inked dot.

els to be assessed for validation. Thus, the indices of a vector were assigned either 1 or 0, indicating the presence or absence of macrophages, respectively; the number of elements in the vector should match the number of A-lines. Likewise, the indices of a vector corresponding to the FLIM row pixels were assigned binary numbers for the presence of macrophages.

Figure 4.4 shows the FLIM lifetime map (A) and the OCT en face image (B) with the binary vector plotted on the corresponding row; the OCT B-scan linked to that row (C); and the related histological image (D) with the lumen marked for macrophage presence using ImageScope. These vectors were used as means to correlate the histological classification to the automatic classification for validation in the statistical correlation and the ROC analyses. The ROC analysis was performed in two ways: A-line/pixel-wise and slice-wise classification.

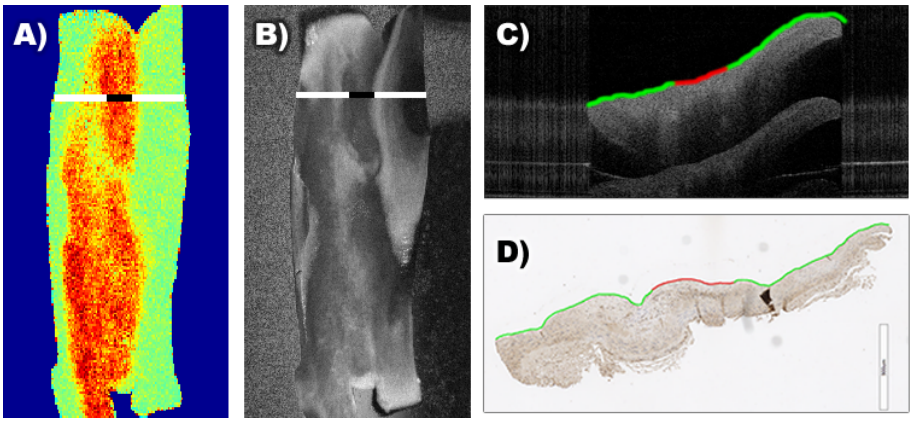

Figure 4.4: Binary index selection based on histology. A) FLIM lifetime map from the second channel and B) OCT en face image with the binary vector plotted on the corresponding row (white positive, black negative); C) the OCT B-scan corresponding to the index of that row with a line plotted on the lumen (red positive, green negative); D) the Histological image belonging to that index with the lumen marked for macrophage presence (red positive, green negative).

4.4 Results

4.4.1 OCT macrophage identification results

A set of areas under the ROC curve was used to find the optimum size for the moving filter. Each ROC curve was constructed by plotting the true positive rate against the false positive rate produced by the classification of the 7 artery segments using different sizes. The height and width of the filter and the separation span had the same magnitude for each size evaluated. Figure 4.5(A) depicts the areas for different sizes ranging from 21 to 61 pixels (147 μm to 427 μm). Since filter sizes larger than 45 pixels did not show significant improvement, the optimum filter size and span were set to 45 pixels (315 μm). The ROC curve for a size of 45 pixels is shown in Fig. 4.5(B). The NSDRatio threshold of 3.4 a.u had the highest accuracy of 79.09% with a sensitivity and specificity of 79.25% and 79.04%, respectively.

Figure 4.6 shows the NSDRatio classification result of the OCT images of an artery

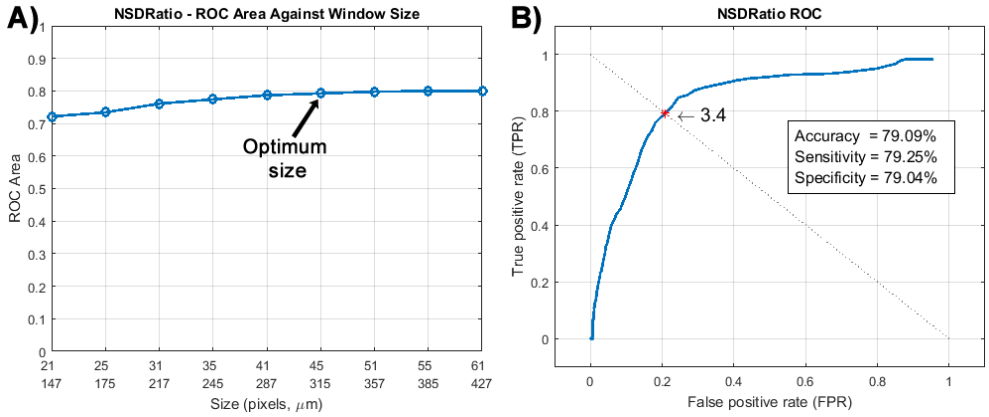

Figure 4.5: A) Areas under the ROC curve for different filter sizes. B) ROC curve of the selected optimum size of 45 pixels (315 μm). .

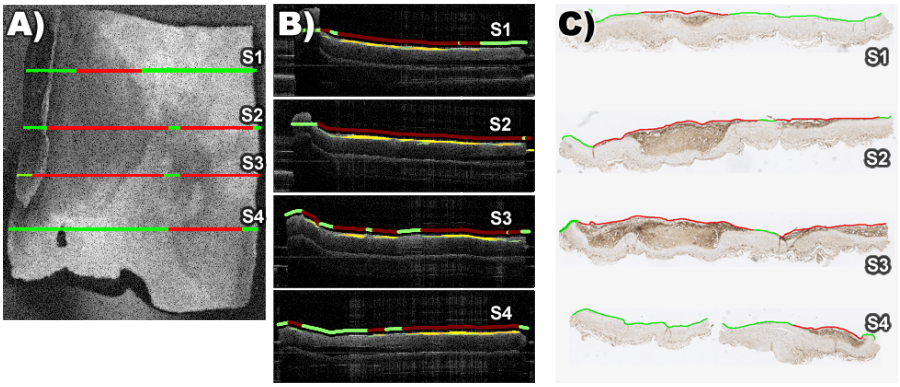

Figure 4.6: NSDRatio classification result of the OCT images of an artery section classified by histopathology as positive for M/FC presence. A) En face OCT image with the histology-based classification lines of each slice (red positive and green negative for M/FC). B) OCT B-scans corresponding to the four histology slices (S1-S4) with the NSDRatio pixels that surpassed the threshold and the indices of the A-lines classified as positive (maroon) and negative (green) plotted on the lumen. C) CD68 images of the four slices with the histology-based classification drawn on the lumen (red positive and green negative for M/FC).

section containing M/FC clusters. The lines on the en face image (Fig. 4.6(A)) indicate the histology-based classification for each slice (S1-S4), where the color red and green indicate positive and negative for M/FC, respectively. The automated NSDRatio classification

result is shown on the B-Scans corresponding to each histology image by overlaying the pixels of NSDRatio map that exceeded the selected threshold of 3.4 a.u. (see Fig. 4.6(B)). The lines over the lumen represent the binary classification of each A-line, where the colors green and red indicate positive and negative for M/FC presence, respectively. Figure 4.6(C) shows the CD68 images of the four slices with the histology-based classification drawn on the lumen (red positive and green negative for M/FC).

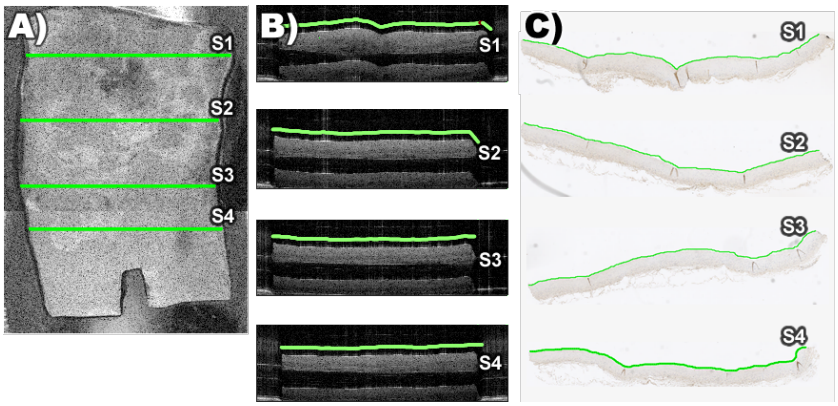

Figure 4.7: NSDRatio classification result of the OCT images of an artery segment classified by histopathology as negative for M/FC presence. A) En face OCT image with the histology-based classification lines of each slice; since no M/FC were identified, only green lines were plotted. B) OCT B-scans corresponding to the four histology slices (S1-S4); no NSDRatio pixels fell above the threshold. Therefore, only green lines (negative for M/FC) were plotted on the lumen. C) CD68 images of the four slices with the histology-based classification drawn on the lumen (green negative for M/FC).

An example of an artery segment without M/FC detected by both histology-base and the NSDRatio classification is shown in Fig. 4.7. The histology-based classification (Fig. 4.7(C)) was negative for all the four slices (S1-S4). In this case, all the values of the NSDRatio map were lower than the threshold. Therefore, no pixels were overlaid on the B-scan by the automated method, and only green lines were plotted on the lumen of each slice (Fig. 4.7(B)).

4.4.2 FLIM macrophage identification results

Since the identification of M/FC in FLIM images is based on a simple threshold applied to the second channel (494 nm), the optimum threshold was found by forming an ROC curve to evaluate the classification result of the 7 artery segments for different thresholds against the histology-based classification or gold standard. Two analyses were performed: per-pixel and per-slice classification. In the first analysis, the binary indices of the histology-based classification were compared against the binary indices of the automated classification obtained from a range of thresholds to form ROC curves (see Fig. 4.8(A)). In the second analysis, a per-slice binary classification was achieved by classifying each histology slice as positive or negative for M/FC presence. In the same way, the corresponding lifetime row was classified binarily by the automated method using a range of thresholds (see Fig. 4.8(B)), where a row was considered positive if at least 10 pixels surpassed the threshold. The per-sample analysis is intended to assess the ability of this method to identify M/FC regardless of the human error in matching the indices of the lifetime row with the indices of the histology-based classification.

The optimum threshold selected from the resultant ROC curves of the per-pixel analysis was $PP\_th_{\tau 2} = 6.8$ ns with an accuracy of 88.94% and a balanced sensitivity and specificity of 90.15% and 88.56%, respectively, while the optimum threshold of the per-sample test was $PS\_th_{\tau 2} = 6.8$ ns with an accuracy of 100%. Thus, this method was able to correctly identify M/FC in each of the slices classified as positive in the histology-based classification. The accuracy of the per-pixel test was slightly lower due the matching error between the histology-based classification segments and the pixel indices of the FLIM map.

A linear correlation plot in Fig. 4.9(A) shows the relationship between the percentage detected by the histology classification and the percentage detected by the automatic

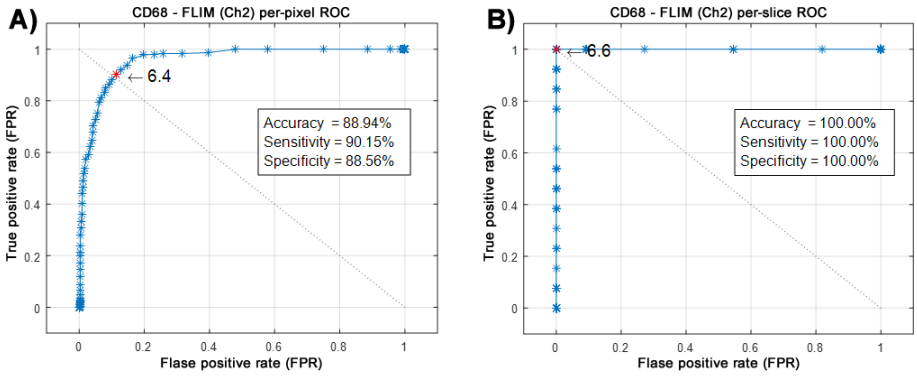

Figure 4.8: ROC curves built from the per-pixel (A) and per-slice (B) classification analysis. The per-pixel test gave the highest accuracy of 88.94% with a sensitivity and specificity of 90.15% and 88.56%, respectively, using a threshold of $PP\_th_{\tau 2} = 6.4$ ns. The per-slice test showed an accuracy of specificity 100% with a threshold of $PS\_th_{\tau 2} = 6.8$ ns, which means that this method matched correctly with the histology-based classification in the per-slice test.

classification using the per-pixel selected threshold $PP\_th_{\tau 2} = 6.8$ ns. The values of the correlation coefficients $R = 0.82$ and $P < 0.05$, for a 95% confidence interval, prove that these two classifications are significantly correlated.

Figure 4.10 shows an example of an an artery section classified by histopathology as positive for M/FC presence. Three slices were cut and stained with CD68 (Fig. 4.10(C)) to identify the presence of M/FC. The red lines on the lumen indicate sections of the artery containing M/FC, while the green represent sections where no M/FC were identified. The lifetime map of the second channel (A) exhibits areas with lifetimes that clearly pass the selected threshold. Therefore, the pixels in those areas were maroon colored by the automated classification method to indicate M/FC presence, while green pixels represent areas without M/FC. The white and black lines on the lifetime and classification maps represent the histology-based classification for each slice (S1-S3); the black and white lines represent positive and negative sections for M/FC, respectively.

Another example for an artery section classified as negative for M/FC presence by

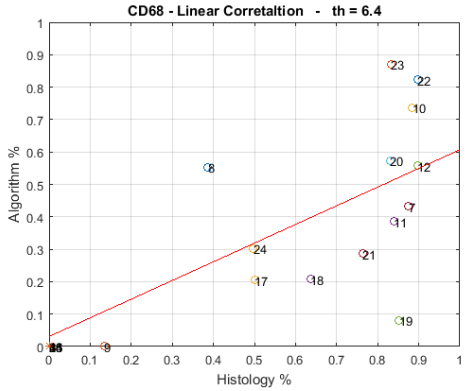

Figure 4.9: ROC curves built from the per-pixel (A) and per-slice (B) classification analysis. The per-pixel test gave the highest accuracy of 88.94% with a sensitivity and specificity of 90.15% and 88.56%, respectively, using a threshold $PP\_th_{\tau 2} = 6.4$ ns. The per-slice test showed an accuracy of specificity 100% with a threshold $PS\_th_{\tau 2} = 6.8$ ns, which means that this method matched correctly with the histology-based classification in the per-slice test.

histopathology is presented in Fig. 4.11. In this case, the three histology slices (S1-S3 in Fig. 4.11(C)) did not exhibit areas with M/FC. Therefore, only green lines were drawn on the lumen of each slice, see Fig. 4.11(C). The lifetime map of the second channel (Fig. 4.11(A)) contains only pixels with lifetimes below the selected threshold. In consequence, the automatic classification method built a homogenous map with only green pixels to indicate that there was no M/FC presence detected.

4.5 Conclusions

The correlation analysis presented in this work demonstrate the ability of bimodality OCT-FLIM imaging to identify M/FC. The NSDRatio applied to OCT images proved an accuracy of 79%, while a simple threshold ($th =\sim 6.4$ ns) applied to the FLIM second channel map showed a higher accuracy of 89% in the automatic identification of M/FC. Thus, the combination of these two approaches can accurately classify and quantify the content of M/FC in OCT-FLIM images of atherosclerotic plaques. Both the NSDRatio

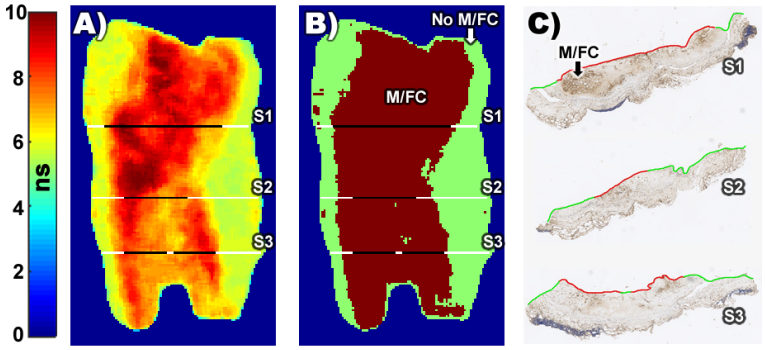

Figure 4.10: Example of an artery section classified by histopathology as positive for M/FC presence. (A) Second channel lifetime map (0 - 10 ns) and (B) classification map (green pixels for no M/FC detected and maroon pixels for M/FC presence). The white and black lines on the lifetime and classification maps represent the histology-based classification for each slice (S1-S3), where black lines represent positive indices for M/FC presence. (C) Histological CD68 stained image, where the red lines on the lumen indicate sections of the artery containing M/FC, and the green lines indicate the lack of M/FC presence.

and the lifetime threshold methods have low complexity and computational cost, so they can be implemented for in vivo discrimination of vulnerable plaques.

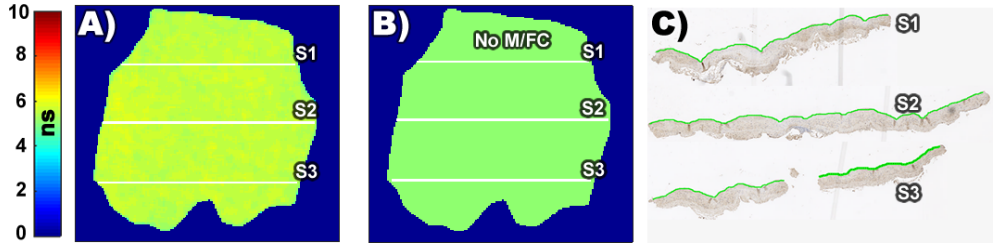

Figure 4.11: Classification result of an artery section classified by histopathology as negative for M/FC presence. (A) Second channel lifetime map (0 - 10 ns) and (B) classification map. In this case, the classification map exhibits only green pixels for no M/FC presence. Likewise, only white lines are shown on the lifetime and classification maps for each slice (S1-S3). Correspondingly, in the histological CD68 stained image (C) only green lines were drawn to indicate that those sections were classified as negative for M/FC presence.

5. APPLICATION OF RAPID LIFETIME DETERMINATION ALGORITHMS FOR CONTINUOUS IN VIVO MULTISPECTRAL FLIM IMAGING BY A FLEXIBLE ENDOSCOPE*

In recent years, interest in the application of fiber-based endogenous FLIM for clinical diagnosis has increased. Likewise, Multispectral wide-field FLIM has been shown to be a robust optical imaging modality for biomedical applications. A fiber-based endoscope combined with an ICCD allows collecting and splitting the fluorescence emission in multiple bands and calculate separately the fluorescence lifetime decay in each spectral channel. However, for accurate calculations, it is necessary to gather multiple gates increasing the imaging time. Since the imaging time is critical for real-time in vivo applications, rapid lifetime determination methods can be employed to considerably shorten this time. To overcome these difficulties, several wide-field time-gated FLIM implementations have been proposed [62, 63, 64, 65, 66, 67]. Time-gated systems divide the fluorescence intensity decay into a defined number of bins and use the integrated intensity of each interval to estimate the lifetime on a pixel-by-pixel basis. Integrating devices, such as ICCDs, help to implement methods that exploit the integration feature. Additionally, the Rapid Lifetime Determination (RLD) methods [68, 69, 70, 71] provide a significantly faster calculation, with slightly lower precision, than traditional multiple gating methods by utilizing fewer gates, which makes it suitable for in vivo imaging.

There are several methods for lifetime determination based on the histogram of the area under the decay curve. These time-gated methods are differentiated by their width, number, and position of the bins. The fluorescence lifetime maps are formed on a pixel-

* Reprinted with permission from "Flexible endoscope for continuous in vivo multispectral fluorescence lifetime imaging" by S. Cheng, J. J. Rico-Jimenez , J. Jabbour, B. Malik, K. C. Maitland, J. Wright, Y. S. Cheng, J. A. Jo, 2013. Optics Letters, 38(9), p. 1515-1517, Copyright [2013] by The Optical Society of America.

by-pixel basis from fluorescence intensity images recorded at different gating parameters. The number of gates, gate width, and the time interval between consecutive gates can be optimized for accuracy or speed. The acquisition and calculation time is shorten by reducing the number of gates, while using a larger number of gates the precision is increased. A comparison of rapid lifetime estimation methods revealed that the standard rapid lifetime determination method (SRLD) and the optimized rapid lifetime determination methods (ORLD) that use only two bins provide practically the same level of precision than those that use more than ten bins, but minimizing both the acquisition and lifetime calculation times [69]. Chang and Mycek demonstrated that an optimal gating method using four gates is more precise than the two-gate approach and it is still fast and easy to implement [70]. This four-gate methodology uses a linearized least-squares lifetime determination method on a pixel-by-pixel basis to rapidly map the fluorescence lifetime. Methods mentioned above were implemented and compared to improve the acquisition and lifetime calculation for the multispectral FLIM endoscope.

5.1 Standard rapid lifetime determination method (SRLD)

The main improvement of the SRLD is speed. As described in [68], for single exponential decay of the form:

$$I(t) = A\, e^{(-t/\tau)} \tag{5.1}$$

the area under the decay curve can be split into two contiguous sections (D_0 and D_1) of equal width Δt as shown in Fig. 5.1. Thus, the lifetime and pre-exponential factor A can be calculated using the following equations:

$$\tau = \frac{-\Delta t}{ln\left(\frac{D_1}{D_0}\right)} \tag{5.2}$$

$$A = \frac{D_0}{\tau\left(1 - \frac{D_1}{D_0}\right)} \tag{5.3}$$

Since these parameters are calculated directly from D_0, D_1, and Δt, the algorithm becomes simpler, more compact, and easier to implement than the linear least-squares method, which needs a larger number of data points for the fitting.

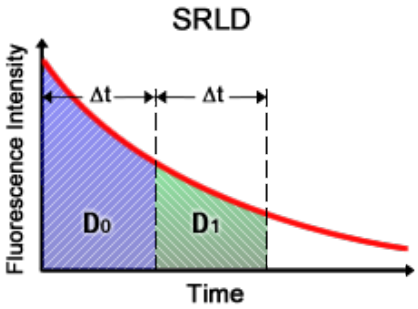

Figure 5.1: Graphic representation of the SRLD method.

5.2 Optimized rapid lifetime determination method (ORLD)

The ORLD method was designed to increase the precision of the SRLD without sacrificing speed [72]. There is no requirement to have periods that are either of equal width or contiguous. Given that premise, two new parameters can be added, Y and P. Y is a fractional delay for D_1 representing a portion of Δt that can take values from 0 to 1, while P is the width of D_1 in units of Δt and can take any value greater than 0. Thus, D_0 runs from t_0 to Δt while D_1 goes from $Y\Delta t$ to $Y\Delta t + P\Delta t$ (Fig. 5.2). Notice that for $Y = P = 1$, the ORLD becomes the SRLD.

A study using Monte Carlo simulations indicated that the ORLD is most precise with $Y = 0.25$ and $P = 12$ [69]. However, this result was based on theoretical comparisons

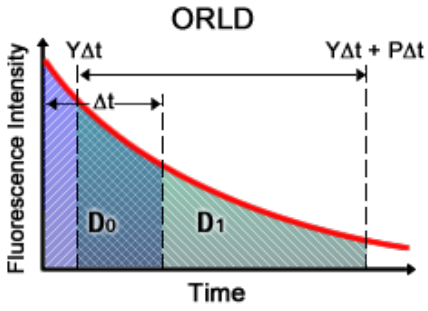

Figure 5.2: Graphic representation of the ORLD method.

of different values of Y and P for the ORLD method. In practice, other factors such as different forms of noise and detector gain affect these parameters.

5.3 Four-gate FLIM method

A promising lifetime mapping technique, which significantly improves the precision in time domain FLIM, shown to be as simple to implement as the two-gate methods, yet somewhat slower [70]. Nevertheless, it is still faster than the multiple gating methods that require at least ten gates for lifetime calculation. In this model, the gate width g and the time interval between the starting points of two consecutive gates t do not change between gates, as shown in Fig. 5.3. New combinations of g and t values are chosen to find the optimal parameters. It uses a linearized least-squares lifetime determination method on a pixel-by-pixel basis to calculate the lifetime τ as:

$$\tau_p = \frac{N\left(\sum t_i^2\right) - \left(\sum t_i\right)^2}{N\sum t_i ln I_{i,p} - \left(\sum t_i\right)\left(\sum ln I_{i,p}\right)} \tag{5.4}$$

Where τ_p is the lifetime of pixel p, $I_{i,p}$ is the intensity of pixel p in image i, t_i is the gate delay of i, and N is the number of gates acquired.

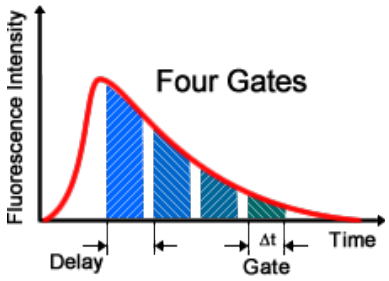

Figure 5.3: Four-Gate FLIM method

5.4 Rapid time-gated FLIM implementation

It has been proved that optimal gating techniques can be used to create fluorescence lifetime maps rapidly using ICCD detectors [67], which makes it very suitable for in vivo wide-field imaging of endogenous fluorophores. Therefore, the aim of this work is to implement and compare the three aforementioned methods to increase the imaging speed of the compact wide-field time-gated FLIM flexible endoscope developed in our lab. This endoscope is capable of continuous lifetime imaging of up to three fluorescence emission channels simultaneously. A schematic of the FLIM endoscopy system is shown in Fig. 5.4. This time-gated system can be configurable for different rapid lifetime determination methods due to its imaging acquisition speed of $\sim$ 2 fps (using SRLD) and an extended minimum gate time down to 200 ps. A frequency-tripled Q-switched Nd:YAG laser provides the excitation light (UV 355 nm, $<$ 1 ns pulse width, maximum repetition rate of 100 kHz). This optics system was set up for imaging of three spectral bands, 390 ± 20 nm, 450 ± 20 nm, and 560 ± 20 nm, based on the emission peaks of three endogenous fluorophores of interest, Collagen, NADH, and FAD, respectively. Combinations of dichroic mirrors, reflective mirrors, and band pass filters allow splitting the fluorescence emission into three spectral channels. The ICCD detector is a 4Picos camera, from Stanford Computer Optics, with a 200 to 800 nm spectral range, 14.4 mm 10.8 mm active area, 780 580

pixels, minimum gate time of 200 ps, 33.8 Hz frame rate.

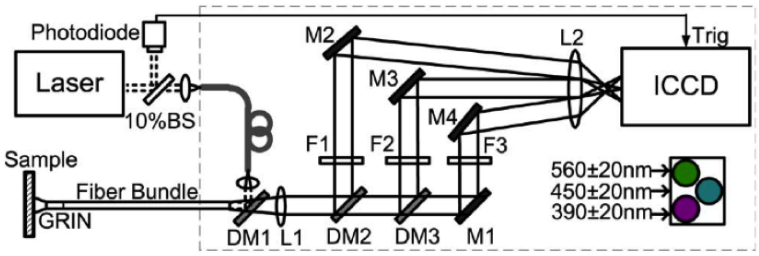

Figure 5.4: Schematic of the FLIM endoscopy system. BS: Beam sampler, DM: Dichroic mirror, M: Mirror, F: Filter, L: Lens.

To achieve real-time imaging, a software tool was developed to implement the two-gate (SRLD and ORLD) and the four-gate protocols and to compare them against the conventional multiple-gate method. The program was developed in LabVIEW for data acquisition, processing, and visualization of three spectral channels. This application can be configurable to work with multiple gating lifetime calculation techniques for rapid lifetime determination using two gates or four gates. This application was specifically designed to control the 4Picos ICCD camera and allow custom time-gated acquisition. Although this software allows tuning of different parameters of the ICCD, the main control parameters for lifetime determination methods are the gate time and delay time. The lifetime mapping was validated by imaging sets of three capillary tubes containing 1 mM solutions of POPOP (diluted in ethanol), NADH, and FAD (both diluted in PBS). The expected emission peaks and lifetimes for POPOP, NADH, and FAD are 390 nm with lifetime of 1.2-1.5 ns, 450 nm with lifetime of 0.3-0.4 ns, and 540 nm with lifetime of 2.3-2.85 ns, respectively [57]. Subsequently, the endoscope was used for in vivo imaging of hamster cheek pouch treated with carcinogenic (DMBA) dyes for oral cancer lesions studies.

Table 5.1: Comparison of the SRLD, Four-gated, and N-gated Lifetime estimation of capillary tubes in nanoseconds.

	450 nm (NADH)	**390 nm (POPOP)**	**560 nm (FAD)**	**450 nm (POPOP)**
N gates (N=20)	0.55 ± 0.71	1.50 ± 0.11	2.49 ± 0.11	1.60 ± 0.20
Four gates	0.63 ± 0.07	0.95 ± 0.17	2.35 ± 0.54	1.09 ± 0.19
Two gates (SRLD)	0.51 ± 0.06	0.93 ± 0.21	2.32 ± 0.56	1.07 ± 0.24
Literature	0.3 - 0.5	1.2 - 1.5	2.3 - 2.8	1.2 - 1.5

5.5 Results

Calibration experiments revealed that using the 4Picos ICCD the SRLD can achieve a lifetime imaging rate of ~ 2 fps, while the rate of the ORLD and four-gated was ~ 1 fps. The ORLD takes longer with only two gates because of the time the ICCD takes to change the gate time. Since the SRLD and four-gated approaches use the same gate time for all their gates this issue is neglected. In terms of lifetime estimation, the SRLD and ORLD showed very similar results. Nevertheless, the ORLD is more complex since it requires finding the optimum values of Y and P. Therefore, the subsequent experiments focused on the comparison of the SRLD and the four-gated methods. Table 5.1 shows a comparison of lifetimes of the capillary tubes obtained with the two-gated SRLD, four-gated, and N-gated methods under the same conditions and the lifetimes reported in the literature [73, 55]. These methods are comparably similar in lifetime estimation but they differ in acquisition speed. The four-gated method requires twice the number of gates than the SRLD, which yields the conclusion that the SRLD is more convenient for this in vivo imaging application.

Figure 5.5 shows the fluorescence intensity and lifetime maps of the capillary tubes from the three spectral channels calculated with the SRLD method. The NADH and FAD fluorescence emissions were observed in the 450 ± 20 nm and 560 ± 20 nm bands, re-

spectively, while POPOP was perceived in both the 390 ± 20 nm and 450 ± 20 nm bands.

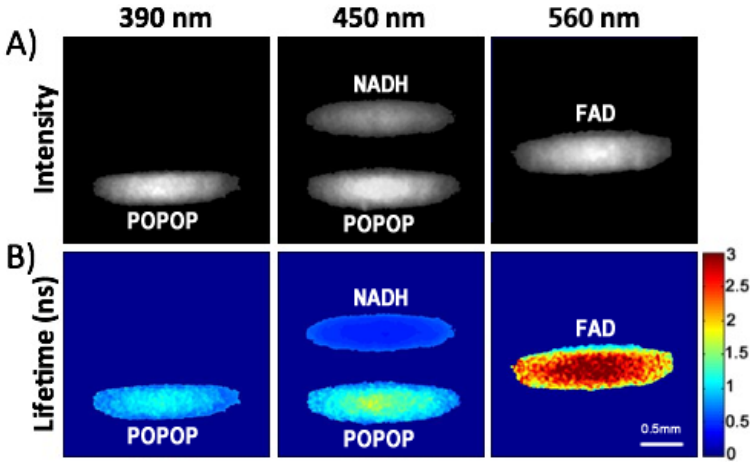

Figure 5.5: In vitro validation imaging of quartz capillaries loaded with (top to bottom) NADH, FAD, and POPOP: (A) fluorescence intensity maps and (B) lifetime maps (color scale in ns).

Likewise, the system was used for in vivo imaging of a hamster cheek pouch lesion that was diagnosed by histopathology as dysplasia. For these experiments, the Institutional Animal Care and Use Committee at Texas A&M University approved the imaging protocol. Figure 5.6 shows the intensity and lifetime maps of the oral lesion that revealed healthy tissue has longer lifetime values compared to the lesion tissue in the 390 and 450 nm channel. The 560 nm channel showed longer values in the lesion area relative to the surrounding healthy tissue. This suggests a stronger emission from NADH and FAD in the lesion area and a stronger Collagen emission in the healthy tissue.

5.6 Conclusions

In sum, this software tool was successfully implemented for a fiber-based FLIM flexible endoscopy system. Simultaneous time-resolved measurement of multiple spectral

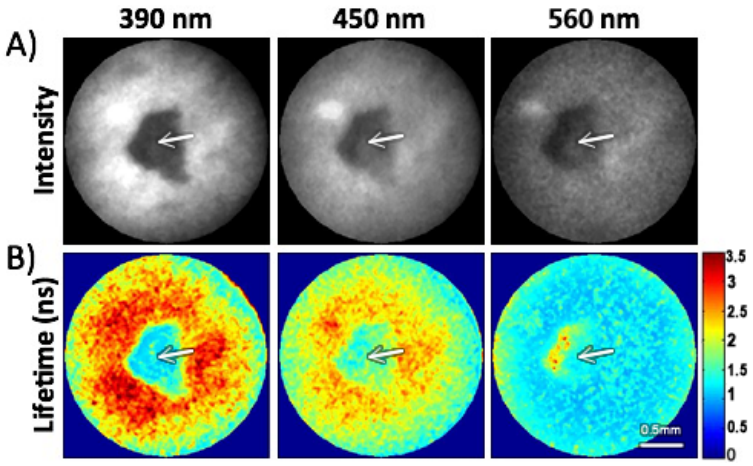

Figure 5.6: In vivo validation imaging of a hamster cheek pouch: (A) fluorescence intensity maps and (B) lifetime maps (color scale in ns). Arrows indicate a small malignant lesion showing distinct fluorescence intensity and lifetime values than those from the surrounding tissue.

bands allows faster multispectral FLIM using the SRLD method, which allows continuous lifetime imaging of up to three fluorescence emission bands simultaneously with a frame rate of $\sim$ 2 fps. Accordingly, this imaging system can be used for multispectral endogenous FLIM imaging for in vivo studies of oral cancer.

6. 3D-2D VISUALIZATION TOOLS FOR INTEGRATION OF OCT-FLIM IMAGING

The surge of dual modality imaging techniques able to simultaneously characterize 3D tissue morphology and biochemical composition of tissue, such as OCT and FLIM, demands enhanced visualization tools to improve the understanding of different stages of atherosclerosis. Plaque thickness, fibrous cap thickness, extension of necrotic core, and calcification are important morphological biomarkers in plaque formation that can be evaluated using 3D high-resolution IV-OCT imaging of atherosclerotic tissue [6]. Analogously, 2D FLIM imaging quantifies intensity and lifetime information obtained from the surface autofluorescence of the lumen to assess relevant biochemical biomarkers, such as the relative content of collagen and lipids within plaques [51, 74]. However, there are no reliable and efficient computational tools for image processing, multimodal imaging integration, and visualization of OCT-FLIM images that allow characterization and early diagnosis of atherosclerosis. OCT and FLIM imaging systems individually provide 3D structural and 2D biochemical tissue information [58, 59, 60], which require adequate integration and visualization tools to properly integrate and exploit them in an effective manner. Therefore, the purpose of this work is to provide computational tools for the integration of dual OCT-FLIM imaging systems to help the characterization of different stages of atherosclerotic tissue by assisting in the identification of the abovementioned morphological and biochemical biomarkers.

The software toolkit presented here has been developed and used as a research tool for studying the progression of atherosclerotic plaques in animal models and ex vivo imaging of human coronary arteries. Furthermore, these tools could eventually be used for in vivo intravascular imaging of human arteries.

This section presents the implementation of combined image processing and visualiza-

tion techniques to help the characterization of 3D morphology and 2D biochemical composition of tissue to improve the understanding of atherosclerotic plaque development, to monitor disease progression, and to even keep track of new medication effects in experimental treatments. This visualization tool provides both a volume rendering view and a textured mapping view for fast slicing through OCT volumetric data, and displaying 2D FLIM mapping of intensity, lifetime, and classification information. As illustrated in Fig. 6.1, in the multimodality imaging integration process, FLIM images are mapped as the surface of the lumen of the OCT volume in a 3D renderer.

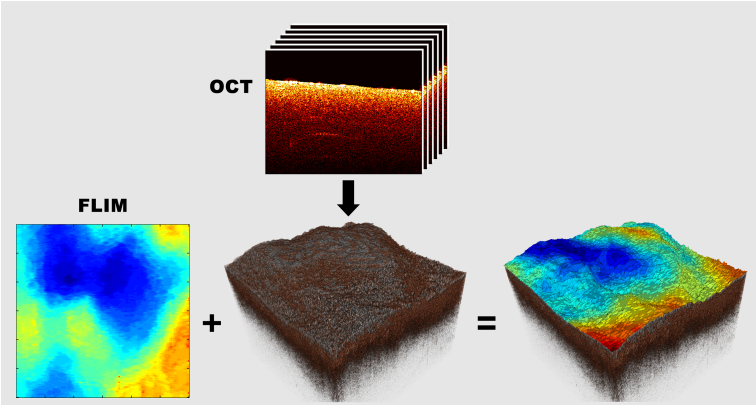

Figure 6.1: OCT and FLIM imaging integration process. The stack of OCT images are rendered as a volume and the FLIM images are mapped as a texture on the lumen surface.

High performance programing languages, for instance C++, hardware-accelerated libraries for image processing and visualization, such as the Visualization Toolkit (VTK), and QT enriched friendly-user interfaces provide a common platform for fast large data image processing and high-resolution 3D and 2D visualization. QT offers a C++ programming environment and a widget integration of VTK to render its 3D environment in the simplest way [75].

6.1 Integration of OCT and FLIM imaging

The process of integrating the 3D and 2D imaging modalities consists of the following steps: OCT lumen surface detection, lumen removal, OCT volume ray casting, plane rendering of volumetric data, surface mesh generation and mapping of FLIM images on the lumen surface, and rendering of separated 2D plane views.

6.1.1 OCT lumen surface detection and lumen removal

Parting from the premise that an OCT volume is constructed by a set of B-scans and one B-scan is formed by a set of A-lines, each B-scan is processed to find its lumen surface line and remove the lumen background signal. Since OCT images are prone to bright line artifacts, each A-line must be equalized to attenuate brighter pixels but to preserve the surface pixels contrast. As shown in Fig. 6.2, the A-line equalization helps to prevent spikes on the detected surface. An A-line y can be equalized as follows:

$$y' = \sum_i \frac{y_i}{\bar{x}_B} \tag{6.1}$$

Where y' is the equalized A-line, i is the pixel index, and $\bar{x}_B$ is the median of the last pixels (20% of the A-line), where the signal attenuation has reached the background.

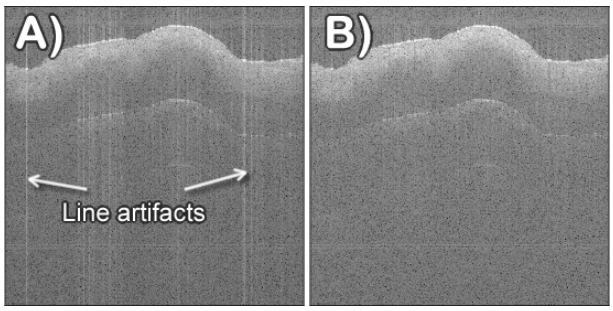

Figure 6.2: Line artifacts removal; A) OCT B-scan with bright vertical lines artifacts and B) B-scan with removed artifacts.

Then, the new B-Scan image is normalized from 0 to 1 and converted to binary using a threshold $th = \bar{x}\delta\sigma$, where $\bar{x}$ and σ are the mean and standard deviation of the whole B-scan respectively; the factor δ controls the number of standard deviations (generally $\delta = 2$). A combination of erode-dilate morphology filters is applied to remove small blobs. The index of the first 1 in each binary A-line is recorded and the resulting vector of indices is smoothed with a median filter. As result, a matrix of indices is created with the surface of all B-scans. All pixels above the surface lines in the original B-scans are set to zero to remove the lumen signal, such that the ray-casting rendering treats them as transparent voxels using proper color and transparency functions.

6.1.2 Surface mesh generation

Once all the lumen surface lines are found, a surface mesh can be generated using common VTK libraries. Basic triangulated surface mesh algorithms are used to generate a wired mesh where the FLIM images will be rendered (see Fig. 6.3). The surface mesh is created with a set of structured vtkPoints in a vtkPolyData class, which represent vertices, lines, polygons, and triangle strips. A vtkDataSetMapper translates the surface as vtkPolyData into graphics primitives in the rendering scene. For those cases where the FLIM image size in pixels does not fit the surface matrix size, a two-dimensional interpolation method must be applied (either nearest, linear, cubic, or spline). The color of each vertex in the surface mesh is set to the corresponding pixel color of the FLIM image. Each time the FLIM image is swapped only the vertex colors are changed on the surface mesh allowing fast rendering.

6.1.3 OCT volume ray casting and plane rendering

OCT imaging is being revolutionized by visualization practices analogous to other imaging techniques, such as MRI, ultrasound, and CT [76, 77]. An enriched 3D visualization environment improves the analysis and characterization of tissue imaging. In

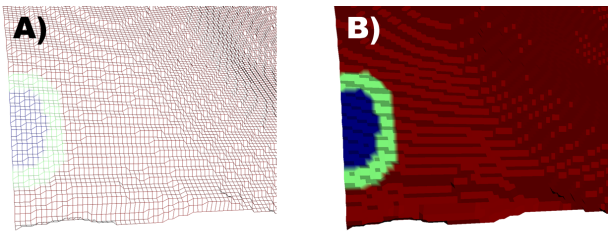

Figure 6.3: Wired (A) and solid mesh (B) of lumen surface.

this visualization tool, a vtkVolumeReader object reads the stack of OCT B-scans creating structured point datasets with the intensity information of each pixel. The reader converts series of 2D slices, in either unsigned 16-bit or 8-bit format, into a 3D volume using a vtkImageData class. Figure 6.4 shows an example of the rendering of ex vivo OCT imaging of human artery tissue with a noticeable degree of fibrosis and thin fibrous cap.

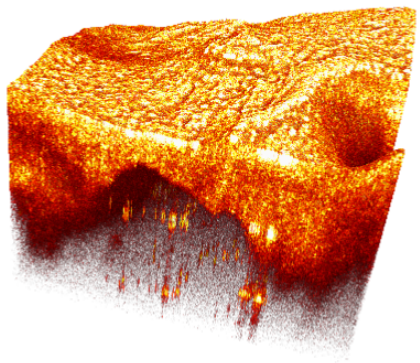

Figure 6.4: Volume ray casting of OCT data.

Then, a vtkVolumeRayCastMapper class renders the volume in the 3D scene. Although custom color functions (colormaps) and transparency functions have been predefined to enhance the color representation of the volume data, the colors and transparencies can be edited in running time to offer more flexibility. Along with the 3D volume, three

planes are constructed from the volume to show different perspectives of the three axes. These image planes work as a reslice cursor that can be manipulated by the user to show the corresponding image at a specific position. The FLIM surface lines are plotted on the image planes to visualize the co-registered FLIM and OCT information. Figure 6.5 shows the sectional planes rendering of the OCT imaging of a human artery with the sectional FLIM lines plotted on the lumen surface.

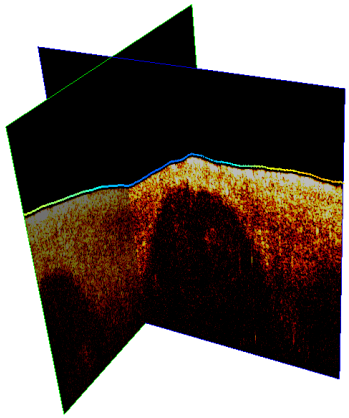

Figure 6.5: Example of sectional planes of OCT volume data.

Axial, sagittal, and coronal planes are additionally rendered in 2D views to give an augmented perspective of the sample and to improve the reslicing feature by changing the slice index with a scrollbar. A supplementary 2D plane view shows the current FLIM image that is mapped as surface on the OCT volume.

6.1.4 Visualization tool extra features

In addition to the common volumetric visualization features, this software provides widgets to show histograms for both FLIM and OCT data, to manipulate the color and transparency functions, and to measure the length or thickness of the sample in the 3D

and 2D views. Since different optical systems may have different resolution, the software can be adapted to show not only the size in pixels but also in the right metric conversion (usually micrometers). As depicted in Fig. 6.6, a metric ruled widget encloses the volume in the 3D scene to show the size of the sample in the three axes, and a measurement tool in the 2D plane view can be used to measure small features in the cross section.

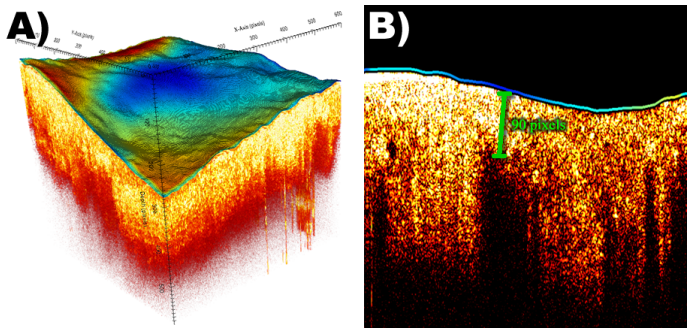

Figure 6.6: Measurement tools; 3D (A) and 2D (B) measurement widgets.

Figure 6.7 depicts the main user-interface components of the visualization software designed for ease manipulation. Multiple widgets provide flexible user interface for effortless interaction and manipulation of the renderers to customize the views, changing different color and opacity functions. The visualizer allows cropping the volume into a region of interest as well as swapping between the whole volumetric data view and the sliced view. Surface image information is plotted over the volume plane views. For FLIM imaging, the lifetime, intensity, or classification maps can be shown as surface.

New maps obtained from the classification methods can be added as surface maps [60, 78]. Additionally, an extra plan view allows visualizing complementary images, such as histology or gross pictures of tissue, in JPEG or PNG formats. Although this visualization toolkit has been designed specifically for OCT and FLIM images, it can be used for any

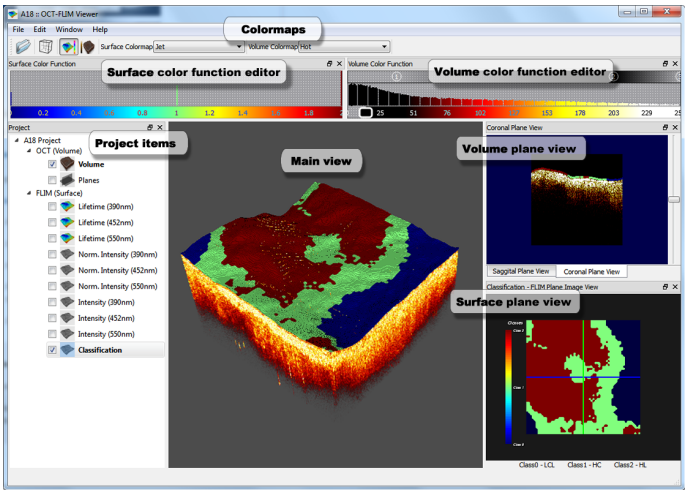

Figure 6.7: OCT-FLIM visualization tool showing different views of an artery dataset.

imaging techniques that require 3D-2D integration.

6.2 Discussion and conclusions

Commercial 3D rendering software is available for volume rendering, such as Amira/ Avizo and Osirix, as well as open source such as ImageJ and 3D Slicer. However, none of them provide tools for the integration of 3D and 2D imaging. The integration of OCT and FLIM imaging was previously performed in Matlab and then rendered using ImageJ, but a separate rendering must be done to visualize each FLIM map on the volume surface, which makes this process very inconvenient. The visualization tool presented here solves this problem by individually rendering the FLIM map on the lumen surface and allowing swapping the surface maps in running time. This software was developed in C++ with a rich user interface provided by QT and 3D rendering environment from VTK libraries. The integration process of the 3D and 2D images consisted of the following steps: OCT lumen surface detection, lumen removal, OCT volume ray casting, plane rendering of volumetric data, surface mesh generation and mapping of FLIM images on the lumen surface, and rendering of separated 2D plane views. This visualization tool was able to individually

render the OCT 3D volume and the 2D FLIM intensity, lifetime, and classification maps. The main advantages of this software was the capability of integrating the two imaging modalities, color functions customization, fast slicing through the OCT volumetric data and the 2D FLIM images, and swapping the FLIM maps on the lumen surface all in running time. This program has been used for the analysis of OCT-FLIM images of human atherosclerotic plaques. This visualization tool covers the minimum needs for the integration of dual 3D-2D OCT-FLIM imaging; yet it can be expanded to provide more robust features as commercial software.

7. SUMMARY AND CONCLUSIONS

In summary, this work provided tools for the image processing, integration, and visualization of OCT-FLIM imaging as well as three innovative classification methods for the characterization of atherosclerotic plaque components, such as lipids, fibrotic tissue and macrophage/foam cells in OCT imaging.

First, a novel computational method for automated tissue characterization of atherosclerotic plaques imaged with IV-OCT based on the modeling of each A-line of an IV-OCT data set as a linear combination of N depth profiles was able to estimate profiles by an alternating least square optimization strategy for an entire pullback segment, and to further automatically classify these profiles to a predefined tissue type. In this study, the proposed method was applied to classify each A-line on an IV-OCT B-scan as Intimal-Thickening, Fibrotic, Fibro-Lipid, or Superficial-Lipid. Such profile classification also allowed the automated classification of IV-OCT B-scans as either Lipid-containing or No-Lipid plaques (overall accuracy of $\sim$85%, compared to $\sim$80% based on visual interpretation by a trained IV-OCT reader). Our encouraging results validated on ex vivo IV-OCT suggest that this methodology has the potential to allow high throughput atherosclerotic plaque assessment through automated tissue characterization.

Ruptured plaques present lesions with a necrotic core, an overlying thin fibrous cap (< 65 μm in thickness), and high macrophage infiltration. For this reason, an automated methodology based on the ratio of a texture feature calculated over two regions was developed. The proposed NSDRatio and ENTRatio approaches increase the sensitivity and specificity of the identification of M/FC clusters compared to the traditional NSD method, which may help to reveal plaque vulnerability. Using the ROC analysis, the NSD showed a classification accuracy of 55.6% while the NSDRatio and ENTRatio showed accuracies

of 86% and 86.9%, respectively. Therefore, the radio concept introduced here may be used to discriminate it between other regions producing high NSD and lacking M/FC. The NSDRatio and ENTRatio have low complexity and computational cost, so they can be implemented for in vivo discrimination of vulnerable plaques.

The correlation analysis presented in this work demonstrated the ability of bimodality OCT-FLIM imaging to identify M/FC. The NSDRatio applied to OCT images proved an accuracy of 79%, while a simple threshold ($th =\sim 6.4$ ns) applied to the FLIM second channel map showed a higher accuracy of 89% in the automatic identification of M/FC. Thus, the combination of these two approaches can accurately classify and quantify the content of M/FC in OCT-FLIM images of atherosclerotic plaques. Both the NSDRatio and the lifetime threshold methods have low complexity and computational cost, so these methodologies can be implemented for in vivo discrimination of vulnerable plaques.

The software tool implemented for a fiber-based FLIM flexible endoscopy system served to assist simultaneous time-resolved measurements of multiple spectral bands to allow faster multispectral FLIM using the SRLD method, which permits continuous lifetime imaging of up to three fluorescence emission bands simultaneously with a frame rate of ~ 2 fps. Accordingly, this imaging system can be used for multispectral endogenous FLIM imaging for in vivo studies of oral cancer.

The integration of OCT and FLIM imaging was previously performed in Matlab and then rendered using ImageJ, however, a separate rendering must be done to visualize each FLIM map on the volume surface, which makes this process very inconvenient. Commercial 3D rendering software is available for volume rendering, such as Amira/Avizo and Osirix, as well as open source such as ImageJ and 3D Slicer. Nevertheless, none of them provide tools for the integration of 3D and 2D imaging. The visualization tool presented here solved this problem by individually rendering the FLIM map on the lumen surface and allowing swapping the surface maps in running time. This software was developed in C++

with a rich user interface provided by QT and 3D rendering environment form VTK libraries. The integration process of the 3D and 2D images consisted of the following steps: OCT lumen surface detection, lumen removal, OCT volume ray casting, plane rendering of volumetric data, surface mesh generation and mapping of FLIM images on the lumen surface, and rendering of separated 2D plane views. This visualization tool was able to individually render the OCT 3D volume and the 2D FLIM intensity, lifetime, and classification maps. The main advantages of this software include the capability of integrating the two imaging modalities, customizing color functions, fast slicing through the OCT volumetric data and the 2D FLIM images, and swapping the FLIM maps on the lumen surface all in running time. This program has been used for the analysis of OCT-FLIM images of human atherosclerotic plaques. This visualization tool covers the minimum needs for the integration of dual 3d-2D OCT-FLIM imaging, but it can be expanded to provide more robust features as commercial software.

REFERENCES

[1] R. Virmani, A. P. Burke, A. Farb, and F. D. Kolodgie, "Pathology of the vulnerable plaque," J. Am. Coll. Cardiol. **47**(8), C13-8 (2006).

[2] M.E. Brezinski, G. J. Tearney, B. E. Bouma, S. A. Boppart, M. R. Hee, E. A. Swanson, J. F. Southern, J. G. Fujimoto, "Imaging of coronary artery microstructure (in vitro) with optical coherence tomography," Am. J. Cardiol. **77**(1), 92-3 (1996).

[3] S. H. Yun, G. J. Tearney, B. J. Vakoc, M. Shishkov, W. Y. Oh, A. E. Desjardins, M. J. Suter, R. C. Chan, J. A. Evans, I. K. Jang, N. S. Nishioka, J. F. de Boer, and B. E. Bouma, "Comprehensive volumetric optical microscopy in vivo," Nat. Med. **12**, 1429-33 (2006).

[4] W. Drexler, M. Liu, A. Kumar, T. Kamali, A. Unterhuber, and R. A. Leitgeb, "Optical coherence tomography today: speed, contrast, and multimodality," J. Biomed. Opt. **19**(7), 071412 (2014).

[5] Z. Sun, "Atherosclerosis and atheroma plaque rupture: imaging modalities in the visualization of vasa vasorum and atherosclerotic plaques," Sci. World J. **2014**, 312764 (2014).

[6] G. J. Tearney, E. Regar, T. Akasaka, T. Adriaenssens, P. Barlis, H. G. Bezerra, B. Bouma , N. Bruining, J. Cho, S. Chowdhary, M. A. Costa, R. de Silva, J. Dijkstra, C. Di Mario, D. Dudeck, E. Falk, M. D. Feldman, P. Fitzgerald, H. Garcia, N. Gonzalo, J. F. Granada, G. Guagliumi, N. R. Holm, Y. Honda, F. Ikeno, M. Kawasaki, J. Kochman, L. Koltowski, T. Kubo, T. Kume, H. Kyono, C. C. S. Lam, G. Lamouche, D. P. Lee, M. B. Leon, A. Maehara, O. Manfrini, G. S. Mintz, K. Mizuno, M. Morel, S. Nadkarni, H. Okura, H. Otake, A. Pietrasik, F. Prati, L. Räber, M. D.

Radu, J. Rieber, M. Riga, A. Rollins, M. Rosenberg, V. Sirbu, P. W. J. C. Serruys, K. Shimada, T. Shinke, J. Shite, E. Siegel, S. Sonada, M. Suter, S. Takarada, A. Tanaka, M. Terashima, T. Troels, S. Uemura, G. J. Ughi, H. M. M. van Beusekom, A. F. W. van der Steen, G. van Es , G. van Soest, R. Virmani, S. Waxman, N. J. Weissman, G. Weisz, "Consensus standards for acquisition, measurement, and reporting of intravascular optical coherence tomography studies: a report from the International Working Group for Intravascular Optical Coherence Tomography Standardization and Validation," J. Am. Coll. Cardiol. **59**(12), 105872 (2012).

[7] T. Kume, T. Akasaka, T. Kawamoto, H. Okura, N. Watanabe, E. Toyota, Y. Neishi, R. Sukmawan, Y. Sadahira, and K. Yoshida, "Measurement of the thickness of the fibrous cap by optical coherence tomography," Am. Heart. J. **152**(4), 755.e1-4 (2006).

[8] H. Yabushita, B. E. Bouma, S. L. Houser, H. T. Aretz, I. Jang, K. H. Schlendorf, C. R. Kauffman, M. Shishkov, D. Kang, E. F. Halpern, and G. J. Tearney, "Characterization of human atherosclerosis by optical coherence tomography," Circulation **106**(13), 1640-5 (2002).

[9] J. Herrero-Garibi, I. Cruz-Gonzalez, P. Parejo-Diaz, and I. Jang, "Optical coherence tomography: its value in intravascular diagnosis today," Rev. Esp. Cardiol. **63**(8), 951-62 (2010).

[10] T. Soeda, S. Uemura, Y. Saito, K. Mizuno, and I. Jang, "Optical coherence tomography and coronary plaque characterization," J. Jpn. Coron. Assoc. **19**(4), 30714 (2013).

[11] L.S. Athanasiou, T.P. Exarchos, K.K. Naka, L.K. Michalis, F. Prati, and D.I. Fotiadis, "Atherosclerotic plaque characterization in optical coherence tomography images," Conf. Proc. IEEE Eng. Med. Biol. Soc. 4485-88 (2011).

[12] A. Prakash, M. Hewko, M. Sowa, and S. Sherif, "Texture based segmentation method to detect atherosclerotic plaque from optical tomography images," Proc. SPIE **8802**, 88020S (2013).

[13] G. van Soest, T. Goderie, E. Regar, S. Koljenovi, G. L. van Leenders, N. Gonzalo, S. van Noorden, T. Okamura, B. E. Bouma, G. J. Tearney, J. W. Oosterhuis, P. W. Serruys, and A. F. van der Steen, "Atherosclerotic tissue characterization in vivo by optical coherence tomography attenuation imaging" J. Biomed. Opt. **15**(1), 011105 (2010).

[14] G. J. Ughi, T. Adriaenssens, P. Sinnaeve, W. Desmet, and J. D'hooge, "Automated tissue characterization of in vivo atherosclerotic plaques by intravascular optical coherence tomography images," Biomed. Opt. Express **4**(7), 1014 30 (2013).

[15] A Karanasos, C Simsek, M Gnanadesigan, NS van Ditzhuijzen, R Freire, J Dijkstra, S Tu, N Van Mieghem, G van Soest, P de Jaegere, PW Serruys, F Zijlstra, RJ van Geuns, and E Regar, "OCT assessment of the long-term vascular healing response 5 years after everolimus-eluting bioresorbable vascular scaffold," J. Am. Coll. Cardiol. **64**(22), 2343-56 (2014).

[16] M. Gargesha, R. Shalev, D. Prabhu, K. Tanaka, A. M. Rollins, M. Costa, H. G. Bezerra, and D. L. Wilson, "Parameter estimation of atherosclerotic tissue optical properties from three-dimensional intravascular optical coherence tomography," J. Med. Imaging **2**(1), 016001 (2015).

[17] C. P. Fleming, J. Eckert, E. F. Halpern, J. A. Gardecki, and G. J. Tearney, "Depth resolved detection of lipid using spectroscopic optical coherence tomography," Biomed. Opt. Express **4**, 1269-84 (2013).

[18] H. S. Nam, J. W. Song, S.-J. Jang, J. J. Lee, W.-Y. Oh, J. W. Kim, H. Yoo, "Characterization of lipid-rich plaques using spectroscopic optical coherence tomography."

J. Biomed. Opt. **21**(7), 7500410 (2016).

[19] J. N. van der Sijde, A. Karanasos, M. Villiger, B. E. Bouma, and E. Regar, "First-in-man assessment of plaque rupture by polarization-sensitive optical frequency domain imaging in vivo." Eur. Heart. J. May **37**(24), 1932 (2016).

[20] O. Marques, *Practical image and video processing using MATLAB* JohnWiley & Sons, Inc., Hoboken, NJ, USA (2011).

[21] A. Lopes, R. Touzi, and E. Nezry, "Adaptive speckle filters and scene heterogeneity," IEEE Geosci. Remote. Sens. Mag. **28**(6), 992-1000 (2002).

[22] A. Maity, A. Pattanaik, S. Sagnika, and S. Pani, "A comparative study on approaches to speckle noise reduction in images," Comput. Intell. and Netw. (CINE), 148-55 (2015).

[23] M. Rivera, O. Ocegueda, and J. L. Marroqun, "Entropy-controlled quadratic Markov measure field models for efficient image segmentation," IEEE Trans. Image Process. **16**(12), 3047-57 (2007).

[24] M. Rivera and O. Dalmau, "Variational viewpoint of the quadratic Markov measure field models: theory and algorithms," IEEE Trans. Image Process. **21**(3), 1246-57 (2012).

[25] O. Gutierrez-Navarro, D. Campos-Delgado, E. Arce-Santana, M. Mendez, and J. Jo, "Blind end-member and abundance extraction for multi-spectral fluorescence lifetime imaging microscopy data," IEEE J. Biomed. Health Inform. **18**(2), 606-17 (2014).

[26] J. Bioucas-Dias, F. Condessa, and J. Kovacevic, "Alternating direction optimization for image segmentation using hidden Markov measure field models," Proc. of SPIE-IS&T Electronic Imaging **9019**, 90190P (2014).

[27] J. Jaumot, R. Gargallo, A. de Juan, and R. Tauler, "A graphical user-friendly interface for MCR-ALS: a new tool for multivariate curve resolution in MATLAB," Chemometr. Intell. Lab **76**(1), 101-10 (2005).

[28] F. W. Young, J. de Leeuw, and Y. Takane, "Regression with qualitative and quantitative variables: An alternating least squares method with optimal features," Psychometrika **41**(4), 505-29 (1976).

[29] M. Villiger, E. Z. Zhang, S. k. Nadkarni, W. Oh, B. J. Vakoc, and B. E. Bouma, "Spectral binning for mitigation of polarization mode dispersion artifacts in catheter-based optical frequency domain imaging," Opt. Express **21**(14), 16353-69 (2013).

[30] T. Wang, D. Palucci, K. Law, B. Yanagawa, J. Yam, and J. Butany, "Atherosclerosis: pathogenesis and pathology," Diagn. Histopathol. **18**(11), 461-467 (2012).

[31] P. Libby, "Inflammation in atherosclerosis," Nature **420**, 868-74 (2002).

[32] W. Insull, "The pathology of atherosclerosis: plaque development and plaque responses to medical treatment," Am. J. Med. **122**(1), S3-14 (2009).

[33] J. E. McLaren, D. R. Michael, T. G. Ashlin, D. P. Ramji, "Cytokines, macrophage lipid metabolism and foam cells: Implications for cardiovascular disease therapy," Prog. Lipid. Res. **50**(4), 331-47 (2011).

[34] P. R. Moreno, "The high-risk thin-cap fibroatheroma a new kid on the block," Circ. Cardiovasc. Interv. **2**, 500-502 (2009).

[35] G. J. Tearney, H. Yabushita, S. L. Houser, H. T. Aretz, I. K. Jang, K. H. Schlendorf, C. R. Kauffman, M. Shishkov, E. F. Halpern, and B. E. Bouma, "Quantification of macrophage content in atherosclerotic plaques by optical coherence tomography," Circulation **107**(1), 113-9 (2003).

[36] B.D. MacNeill, I.K. Jang, B.E. Bouma, N. Iftimia, M. Takano, H. Yabushita, M. Shishkov M, C. R. Kauffman, S. L. Houser, H. T. Aretz, D. DeJoseph, E. F. Halpern, and G. J. Tearney, "Focal and multi-focal plaque macrophage distributions in patients with acute and stable presentations of coronary artery disease," J. Am. Coll. Cardiol. **44**(5), 972-9 (2004).

[37] C. Raffel, G. J. Tearney, D. D. Gauthier, E. F. Halpern, B. E. Bouma, and I. K. Jang, "Relationship between a systemic inflammatory marker, plaque inflammation, and plaque characteristics determined by intravascular optical coherence tomography," Arterioscler. Thromb. Vasc. Biol. **27**(8), 182027 (2007).

[38] A. Tanaka, G.J. Tearney, and B.E. Bouma, "Challenges on the frontier of intracoronary imaging: atherosclerotic plaque macrophage measurement by optical coherence tomography," J. Biomed. Opt. **15**(1), 011104 (2010).

[39] J.E. Phipps, D. Vela, T. Hoyt, D. L. Halaney, J. J. Mancuso, L. M. Buja, R. Asmis, M. Milner, and M. D. Feldman, "Macrophages and intravascular OCT bright spots: a quantitative study," J. Am. Coll. Cardiol. Img. **8**(1), 63-72 (2015).

[40] L. Di Vito, M Agozzino, V. Marco, A. Ricciardi, M. Concardi, E. Romagnoli, L. Gatto, G. Calogero, L. Tavazzi, E. Arbustini, and F. Prati, "Identification and quantification of macrophage presence in coronary atherosclerotic plaques by optical coherence tomography," Eur. Heart. J. Cardiovasc. Imaging **16**(7), 807-13 (2015).

[41] A. Otsu, "A threshold selection method from gray-level histograms," IEEE Trans. Syst. Man. Cybern. **9**(1), 6266 (1979).

[42] F. D. Kolodgie, R. Virmani, A. P. Burke, A. Farb, D. K. Weber, R. Kutys, A. V. Finn, and H. K. Gold, "Pathologic assessment of the vulnerable human coronary plaque," Heart, **90**(12), 1385-1391 (2009).

[43] D. Stamper, N. J. Weissman, M. Brezinski, "Plaque characterization with optical coherence tomography," J. Am. Coll. Cardiol. **47**(8s1), C69-C79 (2006).

[44] S. Uemura, T. Soeda, Y. Sugawara, T. Ueda, M. Watanabe, and Y. Saito, "Assessment of coronary plaque vulnerability with optical coherence tomography," Acta Cardiol. Sin. 30(1): 1-9 (2014).

[45] C. V. Bourantas, F A. Jaffer, F. J. Gijsen, G. van Soest, S. P. Madden, B. K. Courtney, A. M. Fard, E. Tenekecioglu, Y. Zeng, A. F.W. van der Steen, S. Emelianov, J. Muller, P. H. Stone, L. Marcu, G. J. Tearney, and P. W. Serruys, "Hybrid intravascular imaging: recent advances, technical considerations, and current applications in the study of plaque pathophysiology," Eur. Heart J., doi:10.1093/eurheartj/ehw097 (2016).

[46] L. Marcu, M. C. Fishbein, J. M. I. Maarek, and W. S. Grundfest, "Discrimination of human coronary artery atherosclerotic lipid-rich lesions by time-resolved laser-induced fluorescence spectroscopy," Arterioscler. Thromb. Vasc. Biol. **21**(7), 1244-50 (2001).

[47] L. Marcu, Q. Fang, J. A. Jo, T. Papaioannou, A. Dorafshar, T. Reil, J. H. Qiao, J. D. Baker, J. A. Freischlag, and M. C. Fishbein, "In vivo detection of macrophages in a rabbit atherosclerotic model by time-resolved laser-induced fluorescence spectroscopy," Atherosclerosis **181**(2), 295-303 (2005).

[48] L. Marcu, J. A. Jo, Q. Fang, T. Papaioannou, T. Reil, J. H. Qiao, J. Dennis Baker, Julie A. Freischlag, and Michael C. Fishbein, "Detection of rupture-prone atherosclerotic plaques by time-resolved laser induced fluorescence spectroscopy," Atherosclerosis **204**(1), 156-164 (2009).

[49] J. E. Phipps, Y. Sun, M. C. Fishbein, and L. Marcu, "A fluorescence lifetime imaging classification method to investigate the collagen to lipid ratio in fibrous caps of

atherosclerotic plaque," Lasers Surg. Med. **44**(7): 564-571 (2012).

[50] J. Phipps, Y. Sun, R. Saroufeem, N. Hatami, and L Marcu, "Fluorescence lifetime imaging microscopy for the characterization of atherosclerotic plaques," Proc. SPIE Int. Soc. Opt. Eng. , 7161 (2009).

[51] J. Phipps, Y. Sun, R. Saroufeem, N. Hatami, M. C. Fishbein, and L. Marcu, "Fluorescence lifetime imaging for the characterization of the biochemical composition of atherosclerotic plaques," J. Biomed. Opt. **16**(9), 096018 (2011).

[52] H. Fatakdawala, D. Gorpas, J. W. Bishop, J. Bec, D. Ma, J. A. Southard, K. B. Margulies, and Laura Marcu, "Fluorescence lifetime imaging combined with conventional intravascular ultrasound for enhanced assessment of atherosclerotic plaques: an ex vivo study in human coronary arteries," J. of Cardiovasc. Trans. Res. **8**(4), 253-63 (2015).

[53] G. J. Ughi, H. Wang, E. Gerbaud, J. A. Gardecki, A. M. Fard, E. Hamidi, P. Vacas-Jacques, M. Rosenberg, F. A. Jaffer, and G. J Tearney, "Clinical characterization of coronary atherosclerosis with dual-modality OCT and near-infrared autofluorescence imaging," JACC Cardiovasc. Imaging, doi: 10.1016/j.jcmg.2015.11.020 (2016).

[54] S. Dochow, H. Fatakdawala, J. E. Phipps, D. Ma, T. Bocklitz, M. Schmitt, J. W. Bishop, K. B. Margulies, L. Marcu, J. Popp, "Comparing Raman and fluorescence lifetime spectroscopy from human atherosclerotic lesions using a bimodal probe," J. Biophotonics **9**(9), 958-66 (2016).

[55] P. Thomas, P. Pande, F. Clubb, J. Adame, and J. A. Jo, "Biochemical imaging of human atherosclerotic plaques with fluorescence lifetime angioscopy," Photochem. Photobiol. **86**(3), 727-31 (2010).

[56] W. R. Ware, L. J. Doemeny, and T. L. Nemzek, "Deconvolution of fluorescence and phosphorescence decay curves. Least-squares method," The Journal of Physical Chemistry, **77**(17), 2038-2048 (1973).

[57] J. Park, J. A. Jo, S. Shrestha, P. Pande, Q. Wan, and B. E. Applegate, "A dual-modality optical coherence tomography and fluorescence lifetime imaging microscopy system for simultaneous morphological and biochemical tissue characterization," Biomed. Opt. Express **1**(1), 186-200 (2010).

[58] S. Shrestha, B. E. Applegate, P. Pande, and J. Jo, "Design of a dual-modality imaging system using optical coherence tomography and fluorescence lifetime imaging microscopy for anatomical and biochemical diagnosis of tissue," in Proc. SPIE 7554 (2010).

[59] J. Park, P. Pande, S. Shrestha, F. Clubb, B. E. Applegate, J. A. Jo, "Biochemical characterization of atherosclerotic plaques by endogenous multispectral fluorescence lifetime imaging microscopy," Atherosclerosis **220**(2), 394-401 (2012).

[60] J. A. Jo, J. Park, P. Pande, S. Shrestha, M. J. Serafino, J. J. Rico-Jimenez, F. Clubb, B. Walton, L. M. Buja, J. E. Phipps, M. D. Feldman, J. Adame, B. E. Applegate, "Simultaneous morphological and biochemical endogenous optical imaging of atherosclerosis," Eur. Heart J. Cardiovasc. Imaging **16**(8), 910-918 (2015).

[61] S. Shrestha, M. J. Serafino, J. Rico-Jimenez, J. Park, X. Chen, S. Zhaorigetu, B. L. Walton, J. A. Jo, and B. E. Applegate, "Multimodal optical coherence tomography and fluorescence lifetime imaging with interleaved excitation sources for simultaneous endogenous and exogenous fluorescence," Biomed. Opt. Express **7**(9), 3184-3197 (2016).

[62] L. K. van Geest and K. W. J. Stoop, "FLIM on a wide field fluorescence microscope," Letters in Peptide Science **10**, 501510 (2003).

[63] D. S. Elson, I. Munro, J. Requejo-Isidro, J. McGinty, C. Dunsby, N. Galletly, G. W. Stamp., M. A. A. Neil, M. J. Lever, P. A. Kellett, A. Dymoke-Bradshaw, J. Hares, and P. M. W. French, "Real-time time-domain fluorescence lifetime imaging including single-shot acquisition with a segmented optical image intensifier," New J. Phys. 6(180), (2004).

[64] I. Munro, J. McGinty, N. Galletly, J. Requejo-Isidro, P. M. P. Lanigan, D. S. Elson, C. Dunsby, M. A. A. Neil, M. J. Lever, G. W. H. Stamp, P. M. W. French, "Toward the clinical application of time-domain fluorescence lifetime imaging," J. Biomed. Opt. **10**(5), 051403 (2005).

[65] J. McGinty, N. P. Galletly, C. Dunsby, I. Munro, D. S. Elson, J. Requejo-Isidro, P. Cohen, R. Ahmad, A. Forsyth, A. V. Thillainayagam, M. A. A. Neil, P. M. W. French, and G. W. Stamp2, "Wide-field fluorescence lifetime imaging of cancer," Biomed. Opt. Express **1**(2), 627640 (2010).

[66] A. Periasamy and R. Clegg, *FLIM microscopy in biology and medicine*, Taylor & Francis, Boca Raton (2010).

[67] W. Becker, "Fluorescence lifetime imaging–techniques and applications," J. Microsc. **247**(2),119-36 (2012).

[68] R. M. Ballew and J. N. Demas, "An error analysis of the rapid lifetime determination method for the evaluation of single exponential decays," Anal. Chem. **61**, 30-33 (1989).

[69] C. Moore, S. P. Chan, J. N. Demas, and B. A. DeGraff, "Comparison of methods for rapid evaluation of lifetimes of exponential decays," Appl. Spectrosc. **58**(5), 603-7 (2004).

[70] C. W. Chang and M. A. Mycek , "Enhancing precision in time-domain fluorescence lifetime imaging" J. Biomed. Opt. **15**(5), 056013 (2010).

[71] H. C. Gerritsen, M. A. Asselbergs, A. V. Agronskaia, W. G. Van Sark, "Fluorescence lifetime imaging in scanning microscopes: acquisition speed, photon economy and lifetime resolution" J. Microsc. **206**(3), 218-24 (2002).

[72] S. P. Chan, Z. J. Fuller, J. N. Demas, and B. A. DeGraff, "Optimized gating scheme for rapid lifetime determinations of single-exponential luminescence lifetimes," Anal. Chem. **73**(18), 44864490 (2001).

[73] S. Shrestha, B. E. Applegate, J. Park, X. Xiao, P. Pande, and J. A. Jo, "A Novel high-speed multispectral fluorescence lifetime imaging implementation for in vivo applications," Opt. Lett. 35(15), 2558-2560 (2010).

[74] J. Park, P. Pande, S. Shrestha, B. E. Applegate, and J. A. Jo, "Biochemical characterization of atherosclerotic plaques by endogenous multispectral fluorescence lifetime imaging microscopy," Atherosclerosis **220**(2), 394-401, (2012).

[75] W. Schroeder, K. W. Martin, and B. Lorensen, *The Visualization toolkit: an object-oriented approach to 3-D graphics*, 2nd ed. Cliftork, NY: Kitware (1996).

[76] D. Ganguly, S. Chakraborty, M. Balitanas, and T. Kim, "Medical imaging: a review," Commun. Comput. Inf. Sci. **78**, 504-16 (2010).

[77] A. P. James and B. V. Dasarathy "Medical image fusion: A survey of the state of the art," Information Fusion **19**, 4-19.

[78] P. Pande, S. Shrestha, J. Park, I. Gimenez-Conti, J. Brandon, B. E. Applegate, and J. A. Jo, "Automated analysis of multimodal fluorescence lifetime imaging and optical coherence tomography data for the diagnosis of oral cancer in the hamster cheek pouch model," Biomed. Opt. Express **7**(5), 20002015 (2016).